Chemical Science

ROYAL SOCIETY OF CHEMISTRY

REVIEW

View Article Online
View Journal



Cite this: DOI: 10.1039/d6sc00729e

# CPL-active supramolecular polymers

Carmen Atienza, Fátima García and Luis Sánchez *

Supramolecular polymers constitute a highly dynamic and rapidly evolving research field, characterized by the continuous development of systems with increasing structural and functional complexity. Theoretical and mathematical models aimed at understanding the mechanisms of supramolecular polymer formation have played a crucial role in guiding the design of these systems, enabling the discovery of novel assembly pathways and emergent functionalities in both self- and co-assembled architectures. Within this broad landscape, chiral supramolecular polymers occupy a particularly prominent position, as they provide an effective platform for generating well-defined helical structures that can serve as models for the emergence of homochirality in nature while simultaneously enabling a wide range of advanced functional properties. Of particular interest is the incorporation of emissive moieties into the monomeric building blocks of chiral supramolecular polymers, which can lead to the formation of emissive aggregates exhibiting circularly polarized luminescence (CPL). The CPL activity of these systems significantly enhances their relevance across multiple research areas, extending their impact beyond fundamental supramolecular chemistry to applied materials science. This review focuses on representative examples of the diverse strategies employed to obtain CPL-active supramolecular polymers, including the introduction of chiral elements, such as point or axial chirality, into monomeric units, as well as the integration of metallic components. Furthermore, the examples presented demonstrate the high responsiveness of CPL-active supramolecular polymers to external stimuli such as light, solvent polarity and temperature, highlighting their exceptional versatility. These adaptive properties enable the realization of systems with notably high dissymmetry factors ($g_{lum}$) and circularly polarized luminescence brightness ($B_{CPL}$). Finally, this review presents both metallo-organic and purely organic CPL-active supramolecular polymers, together with selected examples of their outstanding applications in areas such as optoelectronic devices, anticounterfeiting technologies, and information encryption.

Received 26th January 2026
Accepted 23rd April 2026

DOI: 10.1039/d6sc00729e

rsc.li/chemical-science



## Introduction

Supramolecular polymers (SPs) are those in which discrete molecules, referred to as monomers, are held together by non-covalent interactions.[1] The first reports on supramolecular polymers date back to the early 1990s from Aida, Lehn and Meijer.[2] The dynamic nature of the interactions through which supramolecular polymers are formed enables applications that require responsiveness, such as adhesives, self-healing materials, drug delivery, optoelectronics and catalysis.[3] When the monomers bear asymmetry elements, these asymmetry can be transferred to the SP leading to the formation of chiral supramolecular polymers.[4] It is worth mentioning that chirality is a geometric property exhibited by a number of chemical compounds, which are chiral if they cannot be superimposed on their mirror image. The most common type of chirality in single molecules comes from the existence of four different substituents on a tetrahedral atom, referred to as a stereogenic centre, such as an $sp^3$ carbon, which can be geometrically arranged in two ways, giving rise to a pair of enantiomers. Enantiomers may exhibit different chemical properties of special interest in areas such as chemical biology and medicinal chemistry. At the molecular level, there are different sources of chirality, including point chirality, which corresponds to asymmetry arising from the presence of stereogenic centres as well as axial and helical chirality, in which a molecule does not possess a stereocenter (such as a chiral carbon) but instead features an axis of chirality, as exemplified by allenes, binaphthyls and helicenes (Fig. 1a). Chirality can also exist at the supramolecular level, for example in helical supramolecular polymers, which can be right or left-handed, depending on the chiral motifs present in their monomeric structure. This occurs when the formation of a one-sided helix is energetically favoured and, therefore, proceeds with an excess of one helical sense over the other.[4]

It is well known that light is an electromagnetic wave, and that the electric field of this wave oscillates perpendicularly to the direction of propagation. In sunlight, the direction of the electric field randomly fluctuates in time and, therefore, it is unpolarized. On the other hand, if the direction of the electric

*Departamento de Química Orgánica, Facultad de Ciencias Químicas Universidad Complutense de Madrid Ciudad Universitaria s/n, 28040-Madrid, Spain. E-mail: lusamar@ucm.es*

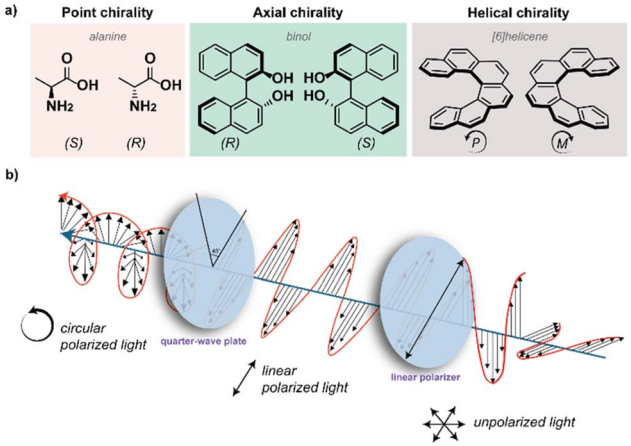


Fig. 1 (a) Examples of chiral molecules bearing different sources of chirality and (b) schematic of the generation of circular polarized light.

field is confined to a certain plane or direction along the propagation direction, the light is polarized. In circularly polarized electromagnetic radiation, the electric field vector is composed of two perpendicular components of equal magnitude that are 90° out of phase. This results in a rotation of the electric field vector around the propagation direction in time, forming a helix that can be right-handed (RCP light) or left-handed (LCP light), yielding what is known as chiral light (Fig. 1b). Chiral molecules can absorb differently RCP or LCP light, thus giving rise to circular dichroism. Analogously, chiral luminogens can emit an excess of RCP or LCP radiation, which generates circular polarized luminescence (CPL). To quantify the CPL emitted by a system, the dissymmetry luminescence factor ($g_{lum}$) is utilized. The $g_{lum}$ parameter is defined as the ratio between the LCP and RCP light intensities ($\Delta I$)[5] emitted and the average intensity ($I_0$) (eqn (1)). $g_{lum}$ expresses the extent of CPL emitted from a system, and its maximum value can vary from −2 to +2, corresponding to 100% RCP and LCP emission, respectively.[6]

$$g_{lum} = \frac{\Delta I}{I_0} = \frac{I_L - I_R}{\frac{1}{2}(I_L + I_R)} \quad (1)$$

Theoretically, in an isotropic medium, $g_{lum}$ is related to the magnetic ($m$) and electric ($n$) dipole moments, and the angle between them ($\theta$) according to eqn (2).

$$g_{lum} = 4\cos\theta \frac{|m|\cdot|n|}{|m|^2 + |n|^2} \quad (2)$$

By analysing eqn (2), it can be concluded that there are some main strategies to attain high dissymmetry luminescence factor values and, therefore, enhance the performance of a CPL emitter. Firstly, a variation in the angle between the magnetic and the dipole moments affects the $g_{lum}$ value. When both vectors are parallel or antiparallel ($\theta = 0°$ or 180°), maximum $|g_{lum}|$ values ($\cos\theta = 1$ or $-1$, respectively) are achieved. Secondly, similar magnitudes of both vectors will also maximize $|g_{lum}|$.

Most organic molecules exhibit low dissymmetry factors ($g_{lum} = 10^{-5}$–$10^{-3}$). In organic molecules with rigid aromatic moieties, the electric dipole transitions are allowed ($\pi \rightarrow \pi^*$), leading to a difference in the $m$ and $n$ values of several order of magnitudes. In contrast, for lanthanide-based complexes, this factor ranges from 0.1 to 1 due to their forbidden electric dipole transitions (4f → 4f).[6b] However, the search for organic systems with enhanced CPL remains significant owing to their ease of processing and low manufacturing costs. The dissymmetry factor has been proven to be enhanced when chiral organic molecules are part of supramolecular assemblies or liquid crystals.

To evaluate the performance of a CPL luminogen, it is not sufficient to evaluate the dissymmetry factor, as it reflects only the relative excess of one handedness of the emitted light and does not consider the total number of circularly polarized photons emitted by the fluorophore. For this purpose, the CPL brightness ($B_{CPL}$) is a parameter that can be employed to compare the performance of different CPL fluorophores as includes the quantum yield ($\phi$), which is the ratio of the number of photons emitted to the number photons absorbed, the molar extinction coefficient ($\varepsilon_\lambda$) measured at the excitation wavelength ($\lambda$), and the absolute $g_{lum}$ value (eqn (3)).[6b]

$$B_{CPL} = \frac{1}{2}\varepsilon_\lambda \cdot \phi \cdot |g_{lum}| \quad (3)$$

Since the $B_{CPL}$ parameter can only be employed for samples in solution, Zinna *et al.* suggested the use of the $B'_{CPL}$ parameter for calculating the CPL brightness of solid-state samples (eqn (4)), similar to the more general brightness parameter $B'$, which is suitable for aggregated, supramolecular and solid-state luminogen samples, where $\varepsilon_{abs}$ is the absorption efficiency, which can be measured using an integrating sphere.[7]

$$B'_{CPL} = \frac{1}{2}\varepsilon_{abs} \cdot \phi \cdot |g_{lum}| \quad (4)$$

The first report on a CPL-active organic compound dates back to 1967 for a bicyclic chiral ketone.[8] Since then, numerous organic and metalloorganic compounds and metal centres have been reported to behave as CPL emitters.[9]

General strategies to obtain materials with elevated CPL efficiency combine a luminescence motif (chiral or achiral), which can be an organic or metallic centre, with a chiral component (*e.g.* point, axial, or helicoidal), and both components should be electronically coupled through covalent or non-covalent interactions. For non-covalent strategies, and in particular for CPL-emissive supramolecular polymers, the efficient luminescence response can come from a metal ion or an aggregation-induced emission (AIE) moiety.[10] Supramolecular polymers exhibiting high dissymmetry factors, as well as covalent polymers, have lower production costs than lanthanide complexes, which are scarce and require highly pure samples, with both factors contributing to increased production costs.

Also, SPs can be designed with a variety of non-covalent interactions, providing wider structural diversity in comparison with liquid crystals. The advantages of supramolecular polymers over covalent polymers for CPL materials are related to their dynamic nature; therefore, their CPL emission can be switched on/off by external stimuli.[11] In summary, the search for supramolecular polymers as efficient CPL emitters is a hot topic in this field.

A key issue in the field of supramolecular polymers is the polymerization mechanism governing the formation of these organized supramolecular entities. There are mainly two types of supramolecular polymerization mechanisms: isodesmic and cooperative or nucleation–elongation. In the isodesmic mechanism, the addition of each monomer to the polymer chain, regardless of chain length, occurs with the same equilibrium constant. In contrast, in the cooperative mechanism, the initial formation of a nucleus is required. This process is described by a nucleation constant ($K_n$). Afterward, more monomers are added to the nuclei to increase the polymer chain length. This second process is described by an elongation constant ($K_e$) and it is thermodynamically favoured in comparison to nucleation ($K_e > K_n$). The difference between both mechanisms has implications in the final properties of the SPs. Thus, isodesmic SPs are more polydisperse and have a lower degree of polymerization than cooperative SPs.[1] When point, axial or helical chiral motifs are included in the chemical structure of the monomeric species, efficient transfer of asymmetry yields chiral SPs. In addition, the formation of chiral SPs can be achieved by an asymmetry amplification process, in which a mixture of two or more monomeric species is utilized. Two strategies can be utilized to achieve an amplification of asymmetry: (i) sergeants-and-soldiers, in which a mixture of an achiral monomeric species and a chiral congener exhibits the same handedness as the pristine chiral system, and (ii) majority rules, in which a mixture of two enantiomers at different ratios causes the enantiomer present in the lower ratio to adopt the handedness of the monomer in excess.[4] In both cases, the transfer of amplification of asymmetry can yield M- or P-type helical SPs showing with high dissymmetry factor values if strong exciton coupling exists. Another important aspect of supramolecular polymerization is pathway complexity, in which the same monomer can lead to different types of aggregates that form through either a consecutive or a competitive regime. In the consecutive process, one aggregate forms first and then serves as a template for the next one, leading to hierarchical organization. In the competitive process, one aggregate must disassemble before another aggregate type can form; therefore, the molecular assemblies in the two aggregates do not need to be related to each other. In terms of CPL, different aggregates can show differences in CPL, such as wavelength, dissymmetry factors, and/or sign. Noteworthy, an emerging concept to attain higher-order aggregates is secondary nucleation,[12] a strategy that has been recently demonstrated as efficient to achieve efficient CPL-active supramolecular polymers.[13]

In the field of CPL-active materials, it should be mentioned that large $g_{lum}$ values for supramolecular gels and solids must be carefully considered because they can be distorted by scattering, linear dichroism (LD)/birefringence (LB), macroscopic alignment, and thickness effects. Therefore, reliable CPL measurements should be accompanied by negligible LD and LB, verification that the signal is independent of sample orientation, and minimized scattering. True CPL spectra should follow the fluorescence profile and remain unchanged with the path length in the non-reabsorbing regime. Instrument calibration with achiral emitters and controls that disrupt supramolecular chirality should yield no signal. Another important issue is to ensure sample purity and optical purity. These precautions help ensure that observed CPL arises from intrinsic chiral emission rather than optical artifacts. Furthermore, a reliable comparison of different parameters related to CPL-active materials ($g_{lum}$, $B_{CPL}$) requires measurements performed at the same wavelength and at the maximum emission intensity.

In this review, we collect relevant and recent examples of CPL-active supramolecular polymers, including both entirely organic and metallo-organic systems, and present supramolecular polymers bearing AIE motifs with point, axial or helical chirality. The CPL activity shown by these chiral supramolecular polymers can be utilized for practical applications, as summarized in the last part of this review. Although there are several reviews dealing with CPL-active materials,[6–9] the present review advances this field beyond prior publications by reframing CPL-active supramolecular polymers not merely as emissive chiral materials but as dynamic, information-rich systems whose optical activity is governed by pathway-dependent self-assembly and hierarchical organization. Earlier reviews catalogue molecular designs, chiroptical performance, and applications, whereas we provide evidence that supramolecular polymerization enables transfer and amplification of asymmetry across length scales, thereby allowing CPL to be programmed through assembly history, external stimuli, and collective behaviour. By presenting concepts such as kinetic *vs.* thermodynamic control and living supramolecular polymerization, we propose a framework in which CPL output becomes a readout of supramolecular information processing rather than a fixed molecular property. This perspective highlights underexplored opportunities, including pathway-encoded CPL states and adaptive and reconfigurable emitters, that could enable next-generation photonic materials, optical data storage, and soft matter systems with learning-like functions. By shifting the focus from structure–property correlations to process–structure–function relationships, this review aims to guide the community toward designing CPL-active SPs as programmable and organized materials, opening new directions beyond conventional molecular engineering.

## CPL-active supramolecular polymers

### CPL-active metallosupramolecular polymers

Chiral coordination polymers with AIE properties are attractive candidates for the design of CPL-active polymer materials. Compared with the corresponding monomeric complexes, chiral coordination polymers generally display much higher luminescence efficiencies and large $|g_{lum}|$ values. Several

examples have been reported based on inorganic cluster-based AIEgens.[14] However, this section focuses on recent advances in the development of metalloorganic supramolecular polymers with tunable CPL properties, with particular emphasis on systems in which metal ions play a crucial role in controlling the assembled nanostructure and the resulting chiroptical activity. From this perspective, one of the earliest examples was reported by Liu in 2019. In this work, Liu and coworkers described a simple fluorophore based on pyrene-conjugated histidine (*L*-PyHis and *D*-PyHis, **1a** and **b**, respectively) in which coordination with metal ions induced a switch in both the self-assembly pathways and the chirality of the resulting supramolecular systems (Fig. 2a).[15] Compounds **1a** and **b** formed gels in the presence of water at room temperature, as confirmed by rheological studies. Initially, they observed different behaviors in the CD and CPL spectra of the gel and the solution states. In the gel, a positive exciton-type bisignate Cotton effect was observed with crossovers at 240 and 353 nm, ascribed to the $^1$Bb and $^1$La bands of pyrene (Fig. 2b), respectively, whereas in solution, the CD signal was practically null.

These CD signals suggest that the chirality localized at the histidine moiety was transferred into the assemblies in the gel. In addition, mirror-image CPL signals were also obtained for the **1a** and **b** gels with an emission band centered at 500 nm, corresponding to the emission peak of the pyrene excimer. SEM and TEM images revealed the formation of nanofibers for the PyHis gel (Fig. 2e). However, the addition of $Zn^{2+}$ to the PyHis gel caused a change in its morphology. The nanofibers were converted into nanospheres when the $Zn^{2+}$/PyHis ratio reached 1 : 5 or higher, as shown by SEM and TEM microscopy (Fig. 2f). Moreover, these nanoparticles were chiral and emissive. Their fluorescence spectra showed that an increase in $Zn^{2+}$ caused the peak ascribed to the monomer emission at 403 nm to increase, while the excimer emission at 500 nm decreased simultaneously (Fig. 2d). Remarkably, as $Zn^{2+}$ increased, the CD and CPL intensities decreased gradually, became silent at a ratio of 1 : 18, and then reversed upon further increase in a reversible manner (Fig. 2c). Back-switching from the PyHis/$Zn^{2+}$ complex to PyHis assemblies could be realized by adding EDTA as a competing ligand. Analysis of the crystal structure by single-crystal X-ray diffraction revealed the possible mechanism of chirality switching and inversion of optical properties. The packing diagram of PyHis indicates a monoclinic structure in which two adjacent pyrene planes are almost perpendicular to each other, forming intermolecular CH-π interactions with a dihedral angle of about 83° between them; this packing mode is almost identical in the gel. Furthermore, the *d*-spacing of 2.23 nm in the PXRD pattern is larger than once but shorter than twice the molecular length of PyHis (1.26 nm), which suggests that two pyrene rings form a structural unit through intermolecular CH-π interactions or T-shaped π-stacking and further self-assemble into nanofibers. Alternatively, for the $Zn^{2+}$-mediated PyHis assemblies, high-resolution mass spectroscopy (HRMS), NMR, and DFT calculations confirmed the formation of a pentacoordinated complex $[(Zn(PyHis)_5]^{2+}$, and the PXRD pattern of $[(Zn(PyHis)_5]^{2+}$ revealed the presence of a peak at 0.35 nm, which implied tight π–π stacking between the pyrene units. This structural change, associated with a dihedral angle of about 90°, favors hydrogen-bonding interactions between the amide functional groups and π-stacking between the pyrene units compared with the PyHis crystals. This large change in the dihedral angle between the two chromophores may lead to the reversal of supramolecular chirality through different spatial arrangements and excitonic coupling interactions. These findings provide mechanistic insights into how metal incorporation induces structural reorganization, thereby altering the self-assembly pathway and causing changes in morphology and CPL response.

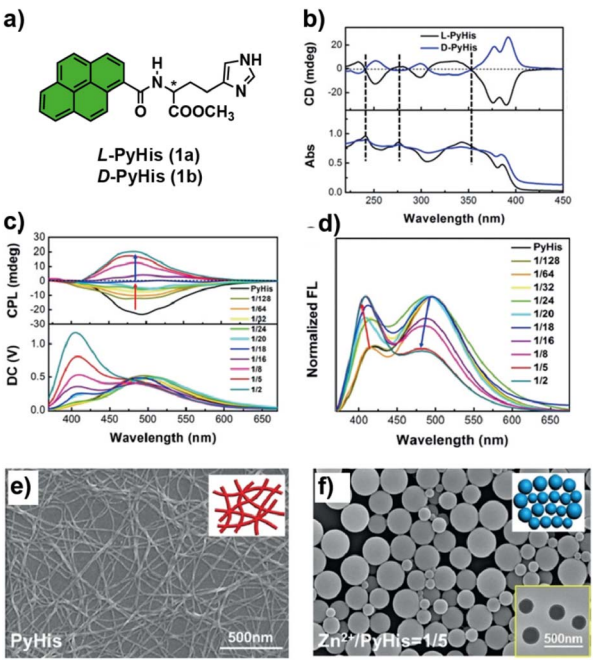


Fig. 2 (a) Chemical structure of chiral PyHis; (b) CD spectra of the **1a** and **1b** gel; (c) CPL spectra and (d) fluorescence spectral change of the **1a** gel in the presence of different amounts of $Zn^{2+}$; (e) morphology transformation detected by SEM of PyHis xero-gel; and (f) SEM image of PyHis in the presence of $Zn^{2+}$; the inserted figure in the bottom right corner is the TEM image of the nanospheres (reprinted from ref. 15 with permission from Wiley-VCH, Copyright 2019).

Multiple approaches for developing CPL-active metal–organic supramolecular polymers (MOSPs) have been reported by G. Liu *et al.*,[16] in which chirality inversion can be induced by modifying the coordinated metal ions, adjusting the solvent polarity, and altering the assembly conditions, including ultrasonic or thermal stimuli. One of these approaches led to the formation of the MOSP pyridine-thiophene-modified cyanostilbene-cholesterol **PTC(2)**, composed of a homochiral pyridine-cyanostilbene-cholesterol molecule that displays multicolor CPL and chirality inversion upon changing the metal ions under specific conditions (Fig. 3).[16b] The chemical structure of **2** consists of a cholesterol moiety, which induces chirality, a thiophene-modified cyanostilbene unit, promoting color-tunable aggregation-induced emission (AIE), and a pyridyl moiety enabling metal coordination (Fig. 3a).[16b] Initial studies showed that pyridine-cholesterol derivatives can be easily

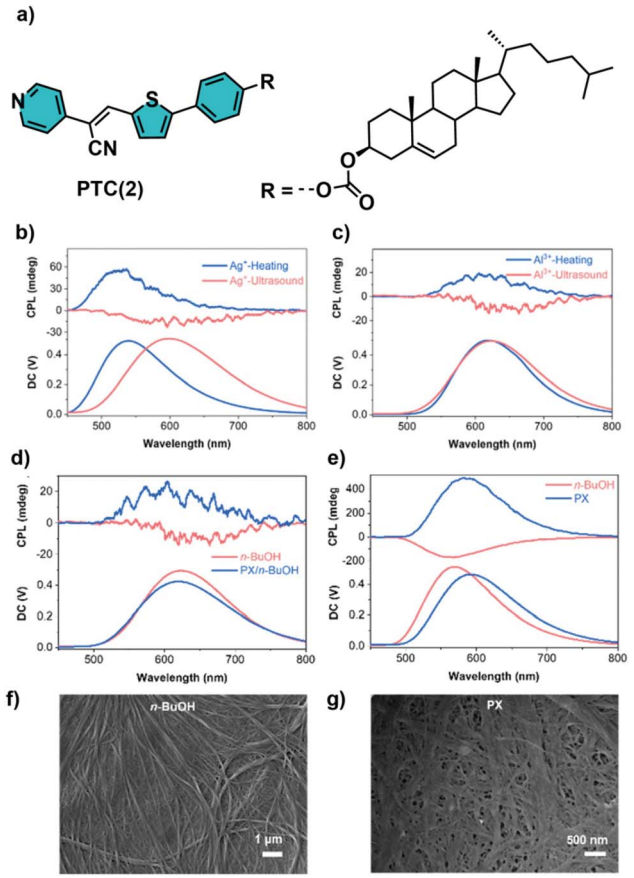


Fig. 3 (a) Chemical structure of the homochiral **PTC(2)**; CPL spectra of **2**-based MOSPs formed by adding (b) $AgNO_3$ and (c) $AlCl_3$ in *n*-BuOH treated with ultrasound (blue line) and a heating-cooling cycle (red line); CPL spectra of **PTC** with (d) $AlCl_3$ and (e) $BiCl_3$ aggregates treated with ultrasound and thermally treated in *n*-BuOH and PX/*n*-BuOH (v/v, 1/1) and PX, respectively; SEM images of PTC + $BiCl_3$ aggregates treated with heating-cooling cycles in (f) *n*-BuOH and (g) PX (reprinted from ref. 16b with permission from The Royal Society of Chemistry, Copyright 2023).

assembled into supramolecular gels under the collective influence of the solvophobic effect and van der Waals forces. The gels exhibited yellow fluorescence with an emission peak at around 540 nm and negative CD and CPL signals at 470–485 nm and 530 nm, respectively. The supramolecular organization was confirmed by SEM microscopy, showing the presence of helical nanofibers. Another scenario arises when derivatives of **2** coordinate with various metal ions. While the coordination with $Fe^{2+}$ and $Fe^{3+}$ promoted gel formation in addition to emission quenching, the addition of different metal ions such as $Ag^+$, $Co^{2+}$, $Cu^{2+}$, $Mn^{2+}$, $Zn^{2+}$, $Bi^{3+}$ or $Al^{3+}$ produced suspensions and $Ag^+$, $Zn^{2+}$, $Bi^{3+}$ and $Al^{3+}$ a red-shifted emission.

Notably, the results from the CD studies demonstrated that chirality inversion was induced by a change in the assembly conditions, specifically ultrasonic or thermal treatment (Fig. 3b and c). Under ultrasonic conditions, **2** + $Ag^+$ and **2** + $Al^{3+}$ exhibited negative CD signals and corresponding right-handed CPL at 595 and 625 nm, respectively. However, upon heating-cooling treatment, both systems displayed positive CD and CPL, suggesting inversion of their supramolecular chirality. In addition, time-dependent CD monitoring indicated that ultrasonic treatment produced kinetically controlled, metastable assemblies, while thermal treatment generated thermodynamically stable structures, exhibiting cation-dependent chirality. Selective CPL studies revealed that **2** + $Bi^{3+}$ exhibited negative CPL at 565 nm, while **2** + $Zn^{2+}$ produced positive CPL at 560 nm, and confirmed the cation-induced CPL inversion. These results indicate that coordination geometry and metal valence dictate the supramolecular stacking modes and chirality outcomes. Another factor that had a significant influence on chiroptical properties was the solvent polarity (Fig. 3d and e). The **2** + $Al^{3+}$ and **2** + $Bi^{3+}$ aggregates treated with ultrasound showed negative CD and CPL signals in polar solvents such as *n*-BuOH; however, a decrease in polarity, such as *p*-xylene/*n*-BuOH (1 : 1) and *p*-xylene (PX), caused signal reversal in both CD and CPL. This inversion was accompanied by a morphological transition from nanofibers (*n*-BuOH) to fused spheres (PX/*n*-BuOH (1 : 1)) and nanoribbons (PX) (Fig. 3f and g, respectively). This strategy developed by Liu *et al.* for constructing multicolor, chirality-switchable metal–organic supramolecular polymers has paved the way for the creation of photomodulated supramolecular polymers for writable information encryption applications, as demonstrated in a recent publication. These authors have also utilized the previously described **PTC(2)**, exhibiting a *Z* configuration for the cyanostilbene moiety, which can undergo *Z*/*E* isomerization and photocyclization upon exposure to ultraviolet or visible light, giving rise to the corresponding complex with an *E* configuration for the cyanostilbene fragment (Fig. 4).[16d] As stated before, ***Z*-2** can self-assemble into a supramolecular polymer in the gel state using various organic solvents, which displays negative CD and CPL signals at 469 nm, and 533 nm, respectively. Initially, these authors showed how **Z-PTC** (***Z*-2**) also exhibited reversible CPL on/off switching and adjustable morphological changes between nanofibrous and fusiform structures upon altering exposure to 454 nm irradiation and heating at 343 K. Interestingly, coordination of ***Z*-2** with silver ions in solvent mixtures, under ultrasonic treatment at room temperature, yields a supramolecular polymer ($SP_1$) with negative CD and CPL signals at 440 nm and 595 nm, respectively, which are distinct from those observed for the nanofibrous aggregate. In addition, time-dependence of the ***Z*-2**/$Ag^+$ supramolecular polymerization was observed with the transformation of the deep yellow solution into yellow flocculent aggregates after 2 h. This transformation suggests that the ***Z*-2**/$Ag^+$ supramolecular polymer can exist in both a metastable state, denoted as metastable $SP_{1m}$, and a thermodynamically stable state, referred to as stable $SP_{1s}$, as confirmed by time-dependent CPL measurements (Fig. 4b). The initially negative CPL sign of metastable $SP_{1m}$ at 595 nm gradually transformed into a positive CPL signal at 525 nm over a 30 min resting period (Fig. 4b). Additionally, the formation of stable $SP_{1s}$ was confirmed by a significant enhancement in the emission observed in the photoluminescence (PL) measurement, accompanied by a change in emission color from orange to yellow (Fig. 4c). The results clearly demonstrate the dynamic assembly of ***Z*-2**/$Ag^+$, forming both metastable and stable

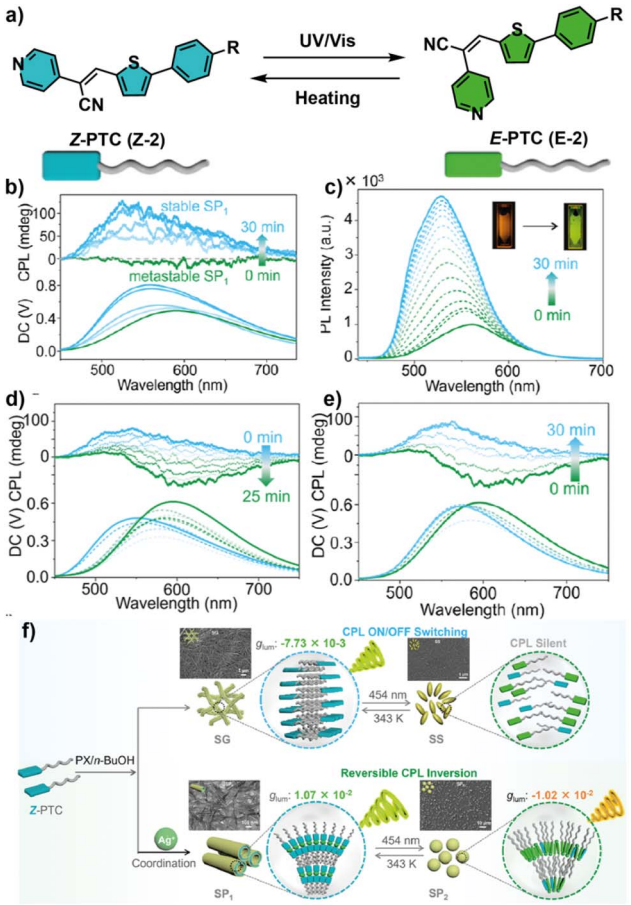


Fig. 4 (a) Reversible *Z*/*E* photoisomerization under 454 nm light irradiation and heating and (b) CPL and (c) PL spectra of ***Z*-2**/$Ag^+$ assemblies in PX/*n*-BuOH. The insets in (c)c show fluorescence photographs of ***Z*-2**/$Ag^+$. (d) and (e) CPL spectra evolution of $SP_1$ obtained (d) under 454 nm irradiation and (e) upon heating at 343 K for different times. (f) Schematic of the CPL reversible transformation process of SG and $SP_1$ under 454 nm irradiation and heating at 343 K, respectively. Inset: SEM images of SG (top) and $SP_1$ (bottom) before and after irradiation, respectively (reprinted with permission from ref. 16d. Copyright 2024, the American Chemical Society).

supramolecular polymers. Moreover, *Z*/*E* isomerization of the ***Z*-2**/$Ag^+$ assembly was studied under 454 nm irradiation monitored by CD and CPL spectroscopy. The initial positive CD and CPL signals of $SP_{1s}$ at 469 and 545 nm gradually shifted to negative signals at 505 nm and 598 nm over a 30 min period upon exposure to the 454 nm light source, respectively (Fig. 4d). These CD and CPL inversions indicate the formation of a new supramolecular polymer, $SP_2$, due to the *Z* to *E* isomerization of the ***Z*-2**/$Ag^+$ complex in a reversible manner upon heating, as shown in Fig. 4e.

The reversible chiroptical inversion was further evidenced by the associated structural transformation observed *via* SEM and transmission electron microscopy (TEM) measurements (Fig. 4f). Initial observation showed nanotubes for $SP_1$, which transformed into nanospheres in $SP_2$ upon exposure to 454 nm light. Intriguingly, nanotubes reappeared after 30-min incubation at 343 K. The result highlights the successful achievement of reversible chiroptical inversion, tunable emission characteristics, and morphological transition of $SP_1$ and $SP_2$ facilitated by 454 nm irradiation and heating at 343 K (Fig. 4f). Upon the introduction of $Ag^+$ ions, the resulting ***Z*-2**/$Ag^+$ complex assembles into laminar structures driven by π–π stacking interactions and hydrophobic effects. The laminar structures subsequently organize into nanotubes with hierarchical chirality transfer and amplification, accompanied by a positive CPL emission at 545 nm, with a $g_{lum}$ value reaching $1.07 \times 10^{-2}$. Irradiation with 454 nm light results in a structural change from the linear ***Z*-2**/$Ag^+$ to a more distorted structure in the ***E*-2**/$Ag^+$ complex. Consequently, the π-stacking interactions may be disrupted, causing the ***Z*-2**/***E*-2**/$Ag^+$ complex mixture to organize into nanosphere aggregates with inversion of the CPL signal at 565 nm and a $g_{lum}$ value of $-1.02 \times 10^{-2}$ (Fig. 4f). Owing to their optical and chiroptical properties, these supramolecular polymers represent promising platforms for aggregated-state multimodal information encryption.

Following this approach, the chiroptical properties of chloride-bridge-linked supramolecular polymers (**3**) can be significantly enhanced by simply decreasing the solvent polarity. In this case, the solvent acts as a modulator inducing intermolecular rotation motion in the dimer, resulting in multiple chiroptical inversion (Fig. 5a).[17] It was observed that, when using *p*-xylene as the solvent rather than dichloromethane, a Zn(II) complex quickly forms, which subsequently aggregates into left-handed microhelices characterized by negative, cyan CPL emission ($g_{lum} = -1.5 \times 10^{-2}$) (Fig. 5b). However, over time, these micro-helices undergo a dynamic transformation into micro-belts with clear reversal of the CPL emission and an increase in the $g_{lum}$ value ($g_{lum} = 5.5 \times 10^{-2}$) (Fig. 5b). Using techniques such as high-resolution electrospray ionization mass spectrometry (HR-ESI-MS) and single-crystal X-ray diffraction, as well as theoretical calculations, they determined that *p*-xylene induces molecular rotation in the **3** dimer, which triggers the formation of distinct crystalline packing structures and dynamic chirality inversion. Furthermore, thermal treatment enhances the rotation of the coordinated complex dimer within the aggregates, leading to a secondary chiroptical inversion and the formation of well-ordered structures. Once equilibrium is reached, a rapid transition in fluorescence from cyan to red was observed upon heating, resulting in a structural transformation from micro-belts to well-ordered nanosheets, as shown in the SEM images (Fig. 5c). Again, this conformational change is accompanied by an inversion of chirality and CPL signal ($g_{lum} = -1.4 \times 10^{-2}$) (Fig. 5b). These outcomes were also observed when xylene isomers, such as *o*-xylene and *m*-xylene, were used as the solvent. In both cases, hydrogen bonding and CH-π interactions facilitate molecular rotation, giving rise to time-dependent CPL inversion. Upon thermal stimulation, cleavage of the chloride bridge is promoted, resulting in a secondary chiroptical inversion accompanied by a tunable shift in CPL emission color. This work provides a versatile platform for developing stimuli-responsive CPL-active systems with dynamically tunable chirality, offering potential for solid-state dynamic encryption applications, as will be discussed in the applications section.

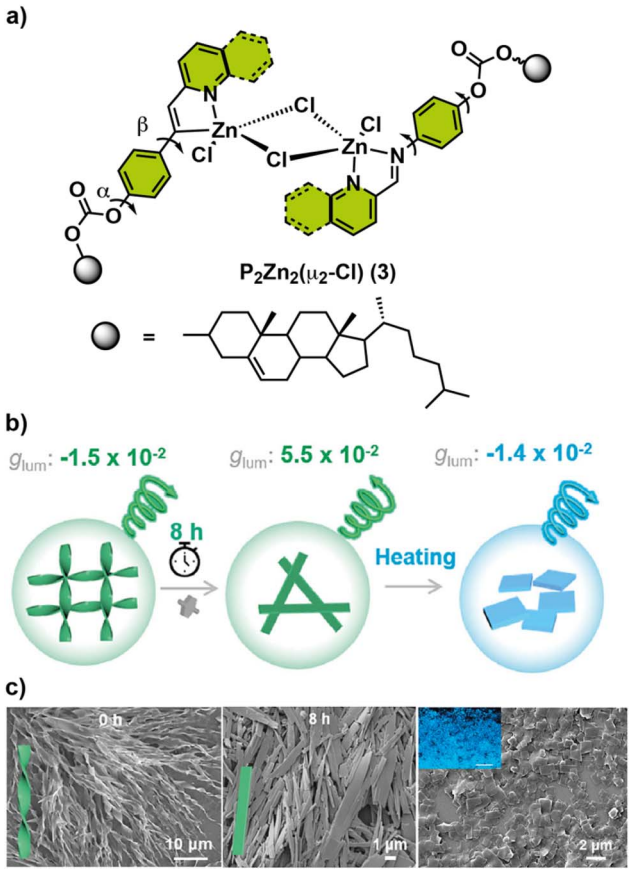


Fig. 5 (a) Chemical structure of the homochiral dimer molecular rotors linked by a chloride coordination bridge. (b) Schematic of the conformation transformation inducing dynamic multiple chirality inversion and tuneable CPL. (c) Time-dependent SEM images of ligand + $ZnCl_2$ aggregates in *p*-xylene at 0 h, 8 h and nanosheets obtained after heating the right-handed micro-ribbons of ligand + $ZnCl_2$ assembly. Inset: fluorescence microscopy image of the nanosheets, with a scale bar of 10 mm (Reproduced from ref. 17a with permission from Wiley-VCH, Copyright 2025).

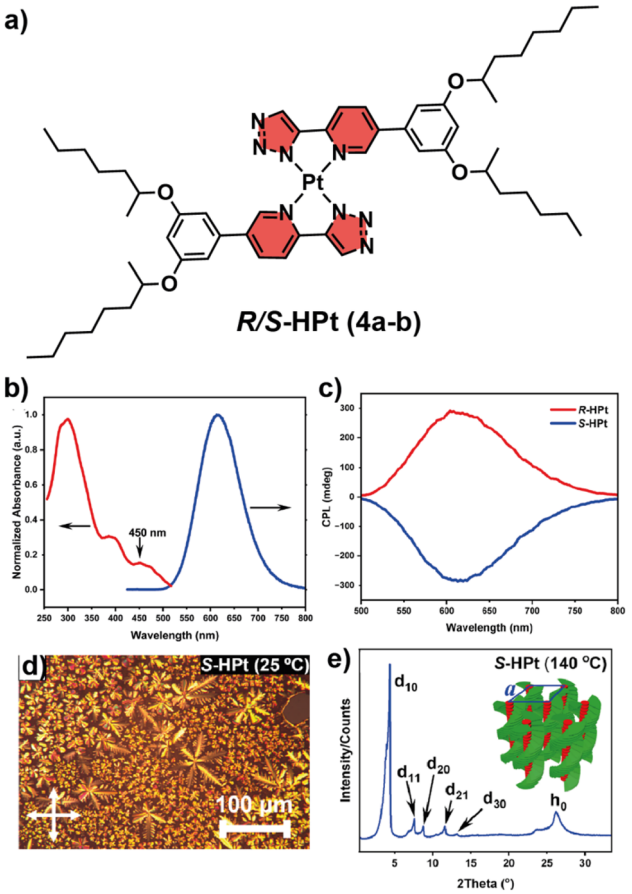


Fig. 6 (a) Chemical structure of homoleptic Pt(II) complexes *R/S*-HPt **4a and b**. (b) Absorption and emission spectra of homoleptic Pt(II) complex T-HPt in spin-coated films; (c) CPL spectra after thermal annealing, (d) POM images of *S*–HPt on cooling and (e) XRD profile of *S*-HPt (reproduced from ref. 18, CC BY).

In contrast to the aforementioned examples, in which metal coordination modulates the optoelectronic properties, an alternative approach involves the deliberate incorporation of a metal center into the molecular design to regulate intermolecular interactions, thereby governing the assembly process. Chen *et al.* created helical columnar emitters *via* thermally induced self-organization mediated by Pt–Pt contacts and π-stacking. They synthesized a pair of enantiomeric homoleptic Pt(II) metallomesogens (*R/S*–HPt) (**4a** and **b**) with chiral pyridine-triazol-based ligands endowed with chiral side chains (Fig. 6a).[18] This flexible side chain, in addition to increase solubility and enantioselective assembly, promotes liquid-crystal behavior. UV-vis absorption and PL measurements reveal distinct spectral features in both solution and thin films. In dilute chloroform, two prominent high-energy absorption bands at 285 and 320 nm arise from the ligand-centered π–π* transition, while weaker low-energy bands at 368 and 383 nm are attributed to MLCT/ILCT processes, which are consistent with the TDDFT analysis (Fig. 6b and c). In spin-coated films, these transitions persist with slight bathochromic shifts (12–14 nm). Additionally, a broad new band emerged near 450 nm, assigned to MMLCT transitions, signifying strong intermolecular Pt–Pt and π-stacking interactions in the solid state. Polarized optical microscopy (POM) measurements show that the enantiotropic hexagonal columnar mesophase is thermally stable. The materials form a highly stable $Col_h$* mesophase (up to 358 °C), exhibiting high photoluminescence PL efficiency ($\phi$ up to 86%) and emitting intense CPL at 615 nm (Fig. 6b and c). When used in solution-processed chiral electroluminescent devices, they achieve high brightness of around 11 379 cd $m^{-2}$. However, remarkably, the electroluminescence dissymmetry factor ($g_{EL}$) increased to 0.014, which is significantly better than many previously reported Pt(II)-based CP-EL systems.

As a final example in this section, we highlight the recent work by Tang *et al.*, in which, in contrast to traditional strategies that rely on the use of opposite enantiomers to achieve inversion of CPL signals, CPL inversion is regulated exclusively through control of the transition dipole moments, without altering the molecular or supramolecular chirality.[19] In this case, they developed new crystal materials based on axially chiral binaphthyl compounds that show solvent-induced CPL

sign inversion. Two chiral Au complexes, (*R*/*S*)-BPAuCz (**R**/**S**)-**5**, based on binaphthyl and carbazole at the terminal positions were synthesized (Fig. 7). Remarkably, both enantiomeric Au-complexes exhibit different properties in solution and in the crystalline state. In THF solution, weak PL was observed for both enantiomers with practically zero quantum yield'; however, the addition of a polar solvent such as $H_2O$ induced a redshift in the emission wavelength of the Au coordination complex, attributed to enhanced intramolecular charge transfer, including ligand-to-ligand charge transfer (LLCT) and ligand-to-metal charge transfer (LMCT). This PL phenomenon suggests that (***R***/***S***)-**5** were aggregation-induced emission active (AIE-active). Besides, no CPL response was observed in a THF solution of (***R***/***S***)-**5**, even upon aggregation in a polar solvent.

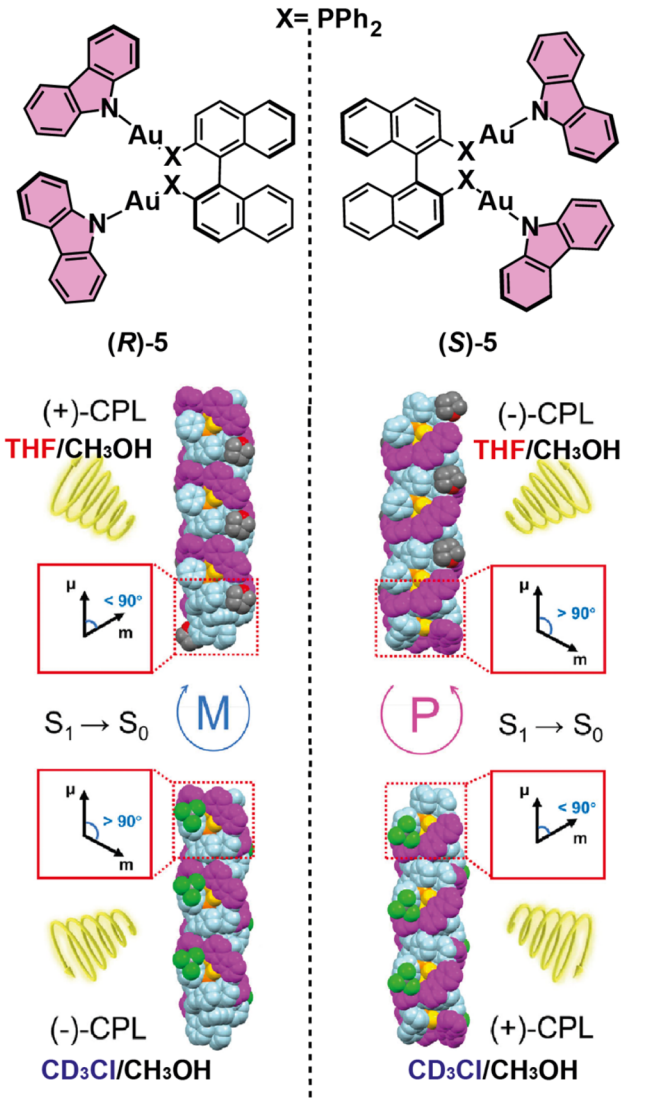


Fig. 7 Helical packing structures, circularly polarized luminescence signs, and transition dipole moment vectors of crystals (*R*/*S*)-**5** crystallized from different mixtures of solvents (THF/$CH_3OH$, upper part of the panel; $CDCl_3$/$CH_3OH$, bottom part of the panel) (reproduced from ref. 19 CC BY).

A different scenario was observed in the crystalline state. Using different techniques, including nuclear magnetic resonance (NMR) analysis, HRMS, and single-crystal X-ray diffraction, it was evidenced that in both enantiomer crystals, two molecules of solvent are present in the crystalline state, THF and $CDCl_3$, respectively. The single crystal of both enantiomers showed mirror-image symmetrical structures between *R*/*S*-stereochemical configurations with a dihedral angle of binaphthyls in the (***R***/***S***)-$\mathbf{5}^{T}$ and (***R***/***S***)-$\mathbf{5}^{C}$ crystals of 90° because of the steric hindrance from the carbazole Au(I) groups linked with 2,2′-binaphthyls. The single crystal of (***R***/***S***)-**5** obtained in THF and $CDCl_3$ exhibited photoluminescence quantum yields higher than those found in the aggregate solution, which were attributed to the tighter molecular packing in the crystalline state, thereby restricting molecular motion. Because of the limited molecular motion, the molecules are strongly emissive in the crystal state. Moreover, CPL sign inversion with the same molecular chirality is observed in the crystalline state depending on the solvent used. The (***R***/***S***)-$\mathbf{5}^{T}$ and (***R***/***S***)-$\mathbf{5}^{C}$ crystals exhibit left-handed CPL with $g_{lum}$ of $+9.81 \times 10^{-4}$ and right-handed CPL with $g_{lum}$ of $-1.02 \times 10^{-3}$ at 560 nm, respectively. These different CPL responses are attributed to the weak interactions between different solvent molecules in the crystal structure, which may affect the transition dipole moments of the bulk crystalline materials. To confirm this hypothesis, TD-DFT calculations revealed solvent dependence with a different angle between magnetic and electric dipole moments ($\theta$ = 86.59° *vs.* 95.89°), respectively, explaining the CPL inversion. Non-bonding interactions between solvent molecules and the AIEgens were found to control these optical properties. Additionally, the crystals demonstrated optical waveguide behaviour, with loss coefficients of 187.3, 567.4, and 65.2 dB $cm^{-1}$ for (***R***)-$\mathbf{5}^{T}$, (***R***)-$\mathbf{5}^{C}$, and (***R***)-$\mathbf{5}^{DCE}$, respectively, showing potential for optical communication and integrated photonic devices.

This section presents an overview of recent developments in chiral coordination polymers displaying CPL activity. These advances contribute to a better understanding of the role of metals as key modulators of optoelectronic properties. Careful consideration of parameters such as metal geometry and valence is essential in the design of these systems, given their critical influence on molecular packing and chirality. In addition, external stimuli can regulate the dynamic behavior of these systems, thereby enhancing their functional properties. The following sections discuss the most significant advances in CPL-active supramolecular polymers, which are organized according to the origin of molecular chirality: point and axial chirality. Factors directly affecting the luminescence dissymmetry factor ($g_{lum}$) are highlighted, including the molecular design of $\pi$-conjugated monomers, the type of supramolecular polymerization mechanism, and the application of different external stimuli.

## Point chirality in CPL-active supramolecular polymers

In CPL-active supramolecular polymers, point chiral monomers serve as essential building blocks that dictate the macroscopic chiroptical properties of the system. Through cooperative self-

assembly mechanisms in which hydrogen bonding, π-stacking, and metal coordination play a crucial role as non-covalent interactions, local point chirality can induce long-range chiral order, leading to enhanced circular dichroism and circularly polarized emission. In this section, we focus our discussion on some strategies in which the application of common external physical stimuli, *e.g.* light and heat, or chemical design can influence the structure organization and tuneable CPL properties of supramolecular polymers.

One of the earliest examples using light to control the macroscopic helical sense of self-assembled structures was provided by Ajayaghosh and coworkers.[20] They demonstrated that the helicity of supramolecular assemblies, defined by their inherent chirality, can undergo a reversible switch to the opposite helical sense through chiral-center-mediated photoisomerization of the appended azobenzenes **6** and **7** (Fig. 8). They synthesized azobenzene-linked phenyleneethynylene (PE) derivatives of **6** and **7** to investigate light- and heat-controlled helical switching supramolecular assemblies. In THF, **(*S*)-7** exhibited monomer-like absorption bands at 324 nm and 419 nm. Upon switching to methylcyclohexane (MCH), these bands were red-shifted to 330 nm and 440 nm, respectively, with an additional shoulder at 480 nm, consistent with aggregation. UV irradiation under MCH conditions induced *trans–cis* photoisomerization, forming mixtures of *E*,*Z* or *Z*,*Z* isomers (Fig. 8a). This transformation was confirmed by the decrease in the absorption intensity at 330 nm, with a slight increase in the absorption intensity at 440 nm and the appearance of two isosbestic points (Fig. 8b). A photostationary state (PSS) is attained within 15 min of irradiation with 53% conversion to the *cis*-isomers (*E*,*Z* and *Z*,*Z*), along with some remaining *E*,*E* isomers. It should be noted that the exact percentage of each isomer in the mixture could not be quantified due to the difficulty in separation by HPLC. Chiral derivatives **(*S*)-7** and **(*R*)-7** showed strong, opposite CD and CPL signals before irradiation, indicating well-defined supramolecular helicity. Surprisingly, upon UV irradiation at 323 K and subsequent cooling, both compounds showed a decrease in intensity and full reversal of their CD signals, demonstrating inversion of supramolecular handedness. The quantitative CD response from the chromophore excitonic coupling was estimated from the dissymmetry factor with $|g_{abs}|$ values of 0.0020 and 0.0022 for **(*S*)-7** and **(*R*)-7**, respectively (Fig. 8b).

Temperature-dependent CD studies reveal a change in the elongation temperature from 310 K to 303 K and a multistep assembly mechanism after isomerization, suggesting the coexistence of aggregates with different isomer compositions. They hypothesized that the initial nucleation may occur with the partially isomerized species present in higher concentration, with inverted helicity, followed by elongation of the helical chain with aggregates of the non-isomerized molecules with the initial *P*-helicity. Upon further cooling, aggregates of the fully isomerized molecules with lower stability and inverted helicity may also join the growing helices, further accelerating the overall opposite handedness. In addition, CPL measurements showed the same tendency after photoisomerization, where the sign of CPL was reversed with a decrease in the $g_{lum}$ value ($g_{lum} = -0.002$ at 503 nm) and ($g_{lum} = +0.002$ at 503 nm) for **(*S*)-7** and **(*R*)-7**, respectively. SEM and AFM imaging confirmed that right-handed (*P*) helical ropes reverse to left-handed (*M*) helices after irradiation, as shown in Fig. 8c and d. Helicity inversion requires heating above 313 K and proceeds through depolymerization followed by reassembly; without heating, irradiation does not change helicity. This process is reversible over multiple switching cycles. A mechanistic model was proposed, in which partially isomerized *E*,*Z* species dominate at the photostationary state and nucleate left-handed aggregates that direct subsequent supramolecular growth. Overall, this study shows that light and heat can reversibly switch the macroscopic helicity of supramolecular assemblies without altering their molecular chirality. This principle is useful for designing responsive materials with switchable optical or electronic properties.

Another pioneering example, described by Kumar *et al.*, demonstrated that bichromophoric systems not only can function as scaffolds to enhance chirality amplification in supramolecular assemblies but also display high CPL emission.[21] They synthesized two *trans*-1,2-diamide-cyclohexane derivatives covalently linked to two chromophoric units of PDIs, differing in the nature of the spacer between them (Fig. 9a). In compound **8**, a glycine unit acts as the spacer, while in compound **9**, β-alanine is the spacer. This subtle increase in the spacer length between the PDI and the cyclohexane moieties helped in reversing the direction of the chiral arrangement of the PDI units connected to the identical chiral center and

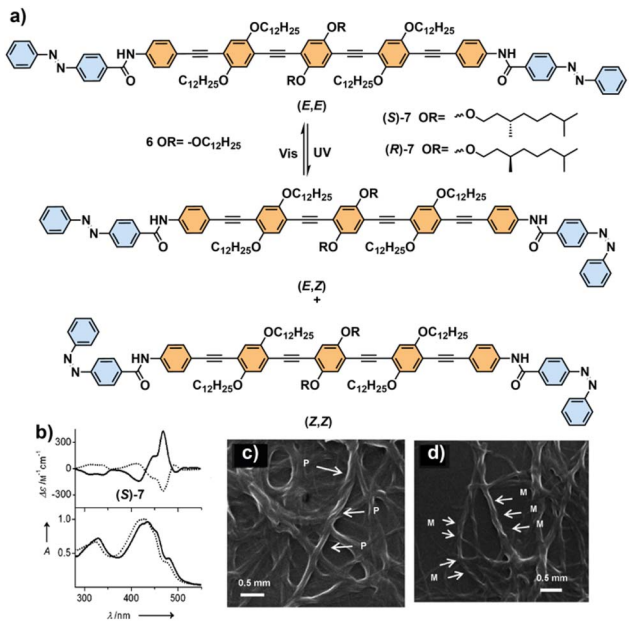


Fig. 8 (a) Photoisomerization of azobenzene-linked phenyleneethynylene derivatives **6** and **7** (*R* or *S*). Mixtures of *E*,*E*; *E*,*Z*; and *Z*,*Z* isomers are possible. (b) CD spectra (top) and the corresponding UV absorption spectra (bottom) for **(*S*)-7** before (dash line) and after (dot line) UV irradiation; (c) SEM images of **(*S*)-7** before and (d) after photoisomerization. (Reprinted from ref. 20 with permission from Wiley-VCH, Copyright 2012).

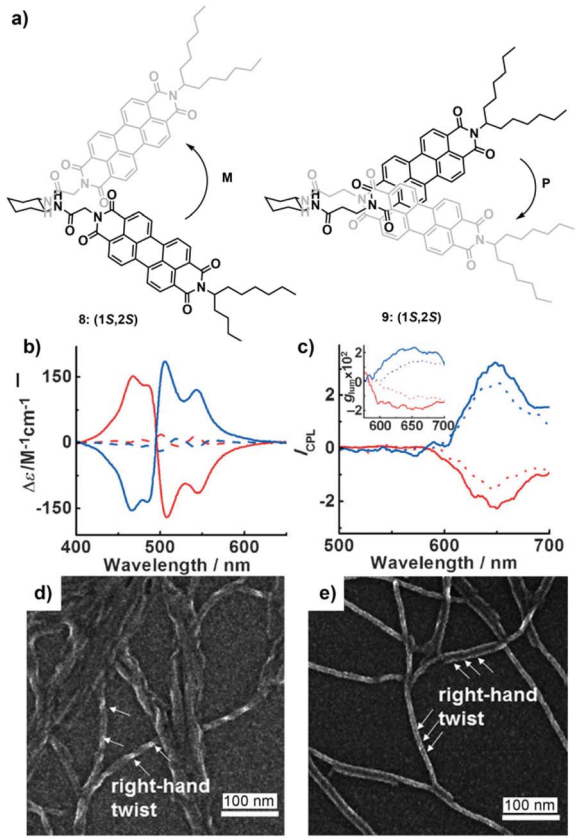


Fig. 9 (a) Molecular structures of compounds **8** (1*S*,2*S*) and **9** (1*S*,2*S*) and schematic of the chiroptical properties in the monomeric and assembled states; (b) CD spectra of the *R* (red lines) and *S* (blue lines) isomers of **8** (broken lines) and **9** (solid lines) in MCH; and (c) CPL spectra of the *R* (red lines) and *S* (blue lines) isomers of **9** in MCH (solid lines) and a chloroform/MCH mixture (dotted lines). The inset in (c) shows the corresponding $g_{lum}$ spectra of **9**. (d) SEM image of (1*S*,2*S*)-**9** and (e) its magnified view (reprinted from ref. 21 with permission from Wiley-VCH, Copyright 2013).

controlled the degree of overlap between the PDI units. Initial UV-vis and fluorescence spectroscopic studies of both molecules in a good solvent such as chloroform indicate that they remain in the monomeric state; however, slight but discernible changes were observed, such as a decrease in the relative absorbance of $A_{0-0}/A_{0-1}$, a more prominent shoulder above the emission at 630 nm characteristic of the excimer-like state, and a longer emission decay for the excimer state in **9** relative to **8**. These differences suggest a stronger overlap of the PDI units in **9**, which also was observed in the CD spectra with an additional strong CD band at 550 nm. Additionally, the chiral nature of the fluorescence was characterized by CPL spectra. The luminescence dissymmetry factor in both compounds at 540 nm matches well with the quantitative CD response from exciton coupling ($g_{lum} = 6 \times 10^{-4}$, $g_{CD} = 4 \times 10^{-4}$) and falls with the typical range reported for such bichromophoric systems in the solution phase. However, in compound **9**, an additional peak with the opposite sign and a large $g_{lum}$ value of $8 \times 10^{-3}$ was observed at 630 nm. This band might be attributed to the decay from the excimer-like state, as suggested by lifetime measurement, which corresponds to the inter-PDI excitation. The CPL sign in the monomeric state correlates with the CD band at the longest wavelength, confirming an intermolecular electronic transition between PDI units governed by their relative P/M configuration. In contrast, excimer CPL exhibits the opposite sign due to a transition dipole oriented perpendicular to the exciton-coupled state. Therefore, the flexibility of compound **9** enhances the CD and CPL responses by increasing PDI–PDI overlap (Fig. 9c and d).

The aggregation behaviour of these PDI-based compounds was studied in $CHCl_3$/MCH mixtures as the solvent. Increasing the MCH content resulted in a redshift in the absorption peak and significant quenching of the monomeric PDI fluorescence emission. This was accompanied by the emergence of a new, intense emission band at a longer wavelength. These outcomes revealed a transition from the monomeric state to aggregates through intermolecular hydrogen bonding and auxiliary π-stacking between the PDI units. Slight differences were also observed in the supramolecular aggregates, with better PDI organization in the self-assembled structures of **9** than **8**, leading to more efficient energy migration, higher emission quantum yield and longer emission lifetime. These aggregates tend to form helical fibres, being more tangled and denser for **8** and more flexible, long and thin for **9** (Fig. 9d and e). It is worth noting that identical helicity was observed in both cases, regardless of the opposite arrangements of perylene moieties in the monomer unit. This fact clearly suggests that the central cyclohexane-diamide unit is responsible for the supramolecular helicity of the self-assembled structures, which was also confirmed by CD spectra. Interesting outcomes were observed, where the CPL of **9** showed $g_{lum}$ values nearly an order of magnitude higher than those of its monomer ($g_{lum} = 0.025$), as well as sign inversion. This value was one the highest reported for organic chromophores in solution at that time. Solid-state CPL studies of the aggregates revealed that **9** formed helical networks of fibrous assemblies, exhibiting an intense CPL signal with a $g_{lum}$ value of 0.035, slightly higher than that observed in solution. This bichromophoric system was one of the first examples in which tuneable chiroptical properties were achieved with large $g_{lum}$ values in solution and the solid state.

Our research group published another example in which a bias in the CPL response occurs, which is directly dependent on the nature of the central π-conjugated unit and the aggregation process.[22] In this case, two pairs of enantiomeric cyanoluminogens (**10** and **11**) based on *p*-phenylene or a 2,5-dithienylbenzene moiety, respectively, as the central chromophore functionalized with four benzamide units, promote supramolecular polymerization through quadruple hydrogen-bonding arrays between the amides and π-stacking of the central aromatic core (Fig. 10). The presence of chiral alkyl side chains induces helicity in the resulting assemblies, making them suitable platforms to explore both kinetically and thermodynamically controlled supramolecular polymerization and the influence on chiroptical and emissive properties. The peripheral benzamide groups can form intramolecular hydrogen-bonded pseudocycles, giving rise to metastable monomers (*M**). These monomers generate kinetically

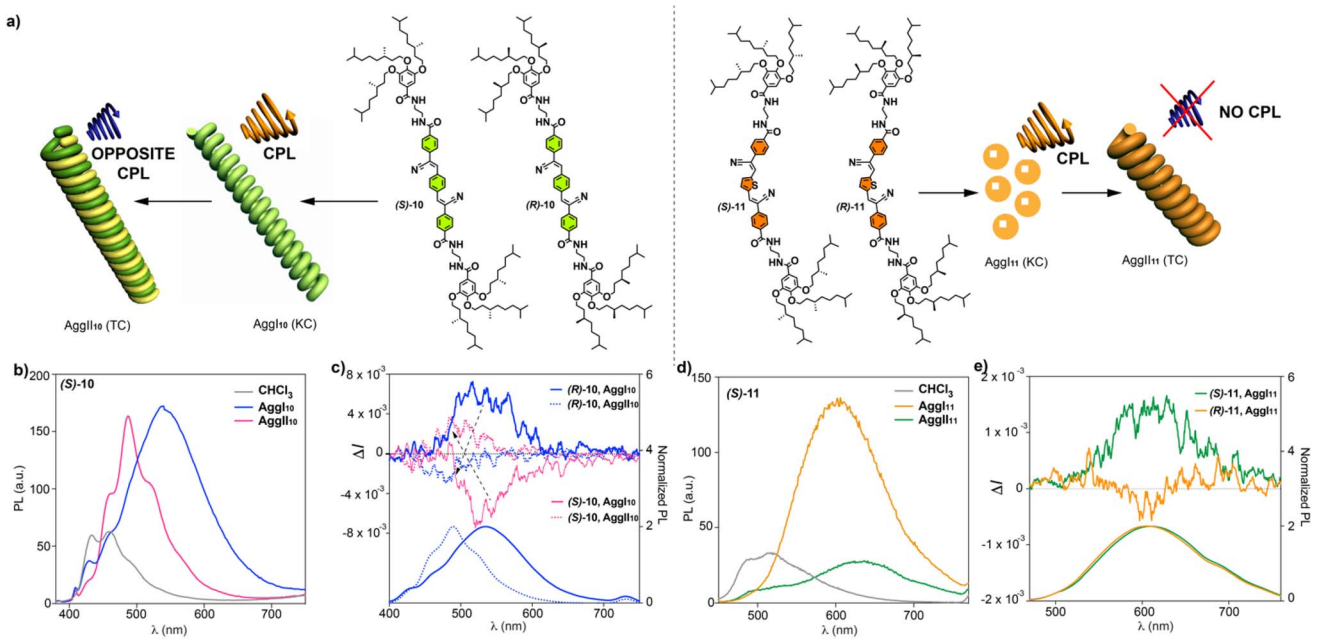


Fig. 10 (a) Chemical structures of chiral cyano-luminogens (representation of the CPL-emitting kinetic and thermodynamically controlled aggregated structures formed by **10** and **11**; PL (b and d) and CPL (c and e) spectra of (*S*)-**10** (left) and (*S*)-**11** (right) in monomeric and aggregated states ($CHCl_3$ and 9/1 MCH/$CHCl_3$ mixture, respectively. Dashed arrows in panel (c) indicate the inversion of the CPL sign (reproduced from ref. 20, CC BY).

controlled aggregates (AggI), which can evolve into more thermodynamically stable aggregates (AggII). The self-assembly process was studied by UV-vis and CD spectroscopy and AFM imaging, revealing distinct aggregation pathways for compounds **10** and **11** (Fig. 10a–e). For compound **10**, AFM confirmed its evolution from thin helical filaments (AggI) into thicker superhelical fibers (AggII). In contrast, compound **11** initially forms nanoparticles (AggI) that reorganize into fibrillar helical structures (AggII), highlighting differences in aggregation driven by the central aromatic unit. CD studies demonstrated that the supramolecular aggregates of both systems are chiroptically active, but their responses depend on the aggregation pathway. Compound **10** showed a bisignate CD response of the same sign for both AggI and AggII, consistent with the formation of helical aggregates. However, compound **11** exhibited a stereomutation phenomenon in which the CD signal inverted its sign during the transition from AggI to AggII, indicating a change in helicity. This stereomutation underscores the sensitivity of supramolecular chirality to kinetic *versus* thermodynamic assembly. The emission properties were also found to be aggregation dependent.

For compound **10**, both AggI and AggII displayed strong photoluminescence due to the AIE effect and significant CPL activity, but with opposite CPL signs between the two aggregate states, as shown in Fig. 10b and c. The value of the dissymmetry factor for these kinetically controlled AggI species was ~0.007 ($\lambda_{exc} = 365$ nm), and aging the solution of AggI for 24 h to ensure its complete conversion to AggII resulted in a sign inversion with a slight decrease in $g_{lum}$ value (~0.004) (Fig. 10b and c). For compound **11**, AggI exhibited strong AIE and detectable CPL, but upon conversion to AggII, the system underwent aggregation-caused quenching (ACQ) and its CPL activity was lost (Fig. 10d and e). These contrasting behaviours demonstrate how subtle changes in molecular design (phenylene *vs.* thienyl core) lead to markedly different emissive and chiroptical outcomes. This work highlights how supramolecular polymerization pathways critically influence the morphology, chirality, and optical properties of chiral cyano-luminogens. While phenylene derivatives **10** maintain their CPL activity with sign inversion between AggI and AggII, thienyl derivatives **11** undergo stereomutation and CPL cancellation upon thermodynamic reorganization. These findings expand the understanding of dynamic supramolecular chirality and show how controlled self-assembly can be harnessed to modulate CPL activity, emission behaviour, and aggregate morphology, with implications for applications in chiroptical devices, sensing, and optoelectronics.

Inspired by systems in nature, where the formation of highly organized helical structures results from multiple interactions governed by cooperative growth, Wang *et al.* designed another more extended π-conjugated system based on a α-cyanostilbene core for the development of CPL detection materials.[23] Two chiral α-cyanostilbene derivatives, (***S*)-12** and (***S*)-13**, were synthesized, with dual amide functionalities flanking the π-core to promote π–stacking and hydrogen bonding through a cooperative growth (Fig. 11a). The (*1S*)-phenylethyl groups imparted point chirality to bias supramolecular helicity. An achiral analogue, compound **14**, was also designed for chirality amplification studies by co-assembly with a small fraction of enantiopure compounds. UV-vis, fluorescence, and

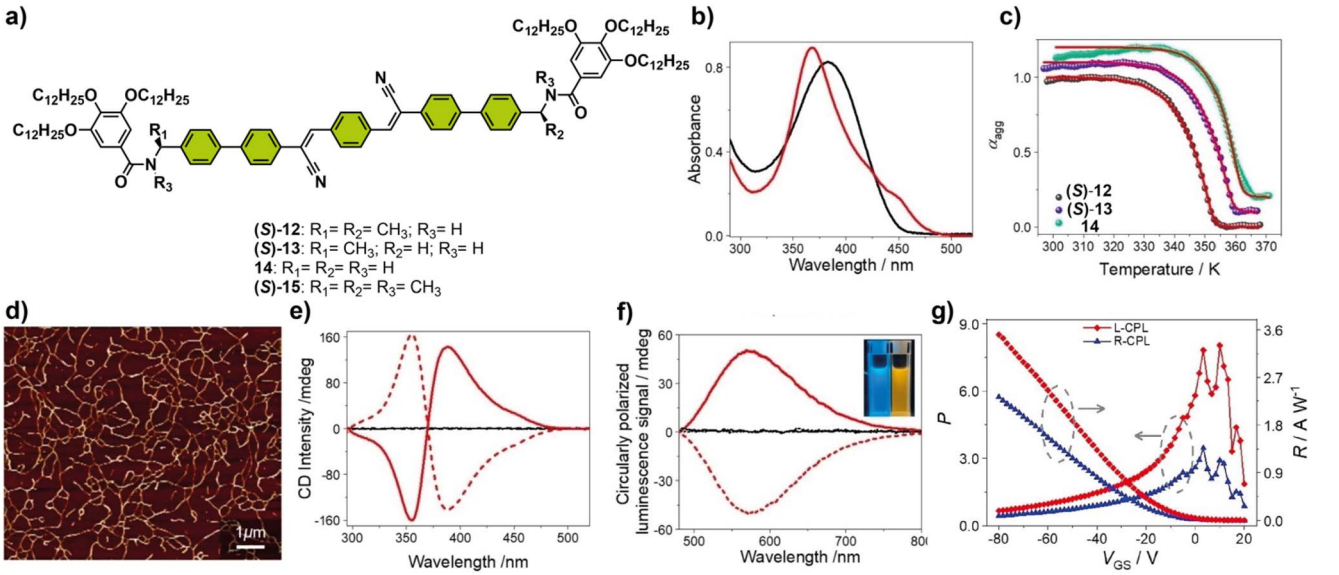


Fig. 11 (a) Chemical structures of the chiral monomers (*S*)-12 or (*S*)-13, the achiral monomer 14 and the control compound (*S*)-15; (b) UV/vis spectra of (*S*)-12 in $CHCl_3$ (black line) and MCH (red line); (c) $\alpha_{agg}$ as a function of temperature for compounds (*S*)-12, (*S*)-13, and 14, by monitoring the absorbance intensity changes at 388 nm; (d) AFM height image of (*S*)-12; (e) CD and (f) CPL spectra of (*S*)-12 (solid red lines) and (*R*)-12 (dash red lines) in MCH. The spectra of the two compounds in $CHCl_3$ are shown in black. Inset of (f): photographs of (*S*)-12 in $CHCl_3$ (left) and MCH (right) under a 365 nm ultraviolet lamp. (g) Photosensitivity (P) and photoresponsivity (R) values of OFETs based on (*S*)-12 supramolecular polymers upon exposure to 450 nm LCP or RCP irradiation (reprinted from ref. 23 with permission from Wiley-VCH, Copyright 2023).

temperature-dependent spectroscopic analyses confirmed cooperative supramolecular polymerization in nonpolar solvent (methylcyclohexane) for (*S*)-**12**, as shown in Fig. 11. In its UV-vis spectrum, a blue shift was observed for the π–π* absorbance band, accompanied by the emergence of a shoulder band between 442 and 500 nm, whilst a red shift from 488 nm to 570 nm was detected for its maximum fluorescence emission signal (Fig. 11b). AFM images revealed the formation of micrometer-long nanofibers, consistent with one-dimensional polymeric growth (Fig. 11d). Supramolecular chirality emerged upon one-dimensional polymerization of **(S)-12** in MCH.

In the π–π* absorption region, a bisignate Cotton signal was detected, consisting of a positive band at 388 nm (anisotropy factor $g_{abs}$ value = 0.00716) and a negative band at 354 nm ($g_{abs}$ = −0.00707). Concurrently, a positive CPL response was observed at 573 nm, yielding a $g_{lum}$ value of $8.3 \times 10^{-3}$ (Fig. 11e and f). In addition, density functional theory (DFT) and FTIR analyses of **(*S*)-12** verified dual noncovalent interactions (π–stacking and H-bonding) as key drivers of its cooperative assembly. In contrast to derivative **15**, in which the amides were methylated, neither supramolecular chirality nor fibrous morphology was detected, despite evidence of π-stacking interactions. Notably, these systems were used to fabricate organic field-effect transistors (OFETs) using poly(3-hexylthiophene-2,5-diyl) (P3HT) as a π-type semiconductor. The **(*S*)-12** devices displayed excellent charge carrier transport capability with threshold voltage ($V_{th}$), maximum field-effect electron mobility ($\mu$), and on/off ratio ($I_{on}/I_{off}$) values of −19.8 V, 0.0044 $cm^2\ V^{-1}\ s^{-1}$, and $8.5 \times 10^4$, respectively. Remarkably, the OFETs based on **(*S*)-12** demonstrated a selective photoresponse with a clear discrimination between left- and right-CPL, yielding a pronounced increase in current and substantial shift in threshold voltage from −19.8 V to −7.8 V under L-CPL illumination. Moreover, the responsivity parameter $g_R$ value of the OFETs based on **(*S*)-12** and **(*R*)-12** were quantified to be +0.83 and −0.82, respectively, which are the highest values observed for π-conjugated supramolecular assemblies. The principal distinction between these systems lies in the supramolecular polymerization mechanism, which follows a nucleation–elongation pathway rather than an isodesmic process.[24] Cooperative polymerization appears to promote a higher amplified dissymmetry factor for circularly polarized photodetectors, driven in part by the enhanced exciton coupling between adjacent α-cyanostilbene units and the size compatibility between the self-assembled polymers and the CPL wavelength, resulting in $g_R$ values for the OFETS exceeding the $g_{abs}$ value of compound **(*S*)-12** in the film state.

Other weaker interactions, such as CH-π, also contribute to the generation of supramolecular systems exhibiting CPL activity. Chiral systems based on styrylpyrene (**(*S*)-16a** and **(*R*)-16b**) utilize this weak interaction to self-assemble into helical nanoribbons *via* cooperative polymerization, preserving their emission properties (Fig. 12).[25] UV-vis and circular dichroism studies revealed that **(*S*)-16a** undergoes cooperative supramolecular polymerization in a solvent mixture such as methylcyclohexane:tetrachloroethane (MCH/TCE, 24 : 1 v/v). Under this condition, a blue shift in the maximum absorption band appears, accompanied by new shoulders at 328 nm and 432 nm, as well as a bisignate cotton effect with positive and negative signals at 392 nm and 356 nm, respectively (Fig. 12b). These

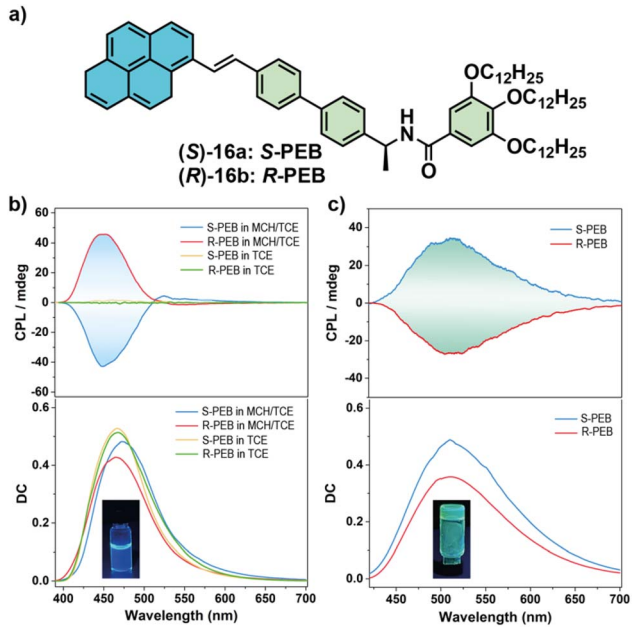


Fig. 12 (a) Structure of *S*-PEB ((***S***)-**16a**) and *R*-PEB ((***R***)-**16b**) monomers and (b) CPL and fluorescence spectra (up and down) of ((***S***)-**16a** and (***R***)-**16b** in MCH/TCE and TCE solutions. Inset: fluorescence image of (***S***)-**16a** in MCH/TCE solution. (c) CPL and fluorescence spectra (up and down) of (***S***)-**16a** and (***R***)-**16b** gel samples formed in a MCH solution. Inset: fluorescence image of the (***S***)-**16a** gel (reported from ref. 25, CC BY).

features indicate π–π offset stacking and the formation of right-handed helicity. In contract to the results in mixed solvents, pure TCE yielded no detectable CD signal. These outcomes unveiled that chirality transfer arises from supramolecular organization. However, variable concentration NMR and fluorescence measurements of (***S***)-**16a** showed no change in the chemical shift of either the amide or aromatic protons, ruling out hydrogen bonding and π-stacking as dominant interactions in the resulting aggregates. Moreover, the emission profiles of (***S***)-**16a** in both its monomeric and aggregated form remained nearly identical, indicating weak electronic coupling between pyrene units. Finally, 2D NOESY spectra confirmed that the aggregates formed exhibit edge-to-face CH-π contacts, as evidenced by the cross-peaks between the phenyl C–H and pyrene protons.

Complementary DFT analyses showed that CH-π interactions dominate the antiparallel twisted stacking mode of (***S***)-**16a** dimers, leading to stable helical supramolecular polymers. This is an exceptional case in which CH-π contacts, rather than π–π stacking or hydrogen bonding, dictate supramolecular helicity. Furthermore, different fluorescence behaviour and a handedness-inverted CPL signal were observed for both enantiomers in solution and the gel state. In solution, aggregated *S*-PEB displayed bright blue fluorescence at $\lambda_{em} = 461$ nm with a high $\Phi_F$ of 69% and a negative CPL signal at 441 nm with a $g_{lum}$ value of −0.001 (Fig. 12b). Alternatively, in the gel state, a yellow-green emission ($\lambda_{em}$ = 498–526 nm and $\Phi_F$ of 39%) was observed due to the stronger packing, along with a positive CPL signal at 510–520 nm ($g_{lum} = +0.0053$) (Fig. 12c). This colour-dependent handedness inversion occurs without inversion of supramolecular chirality, as confirmed by the identical CD spectra for both cases.

Theoretical CPL simulations corroborate that the stacking geometry affects the CPL sign, explaining the opposite handedness between the blue (solution) and yellow-green (gel) states. This behaviour of dual CPL handedness without chirality inversion is exceptionally rare in single-component systems. Moreover, drop-cast and PMMA-embedded films were prepared and showed strong yellow-green CPL with $g_{lum} = +0.001$ and $\Phi_F$ of 26%, consistent with the gel state. The CPL sign is preserved across the gel, film and PMMA composite forms, demonstrating structural stability and reproducibility. This work established a versatile strategy for multi-modal, colour-switchable CPL materials using a single chiral chromophore. Furthermore, the study of the photoreactive behaviour of helical supramolecular polymers derived from stilbene-pyrene presented an additional advancement. Supramolecular confinement provides spatial proximity of the classical photoactive double-bond moieties. This causes the photoinduced [2 + 2] cycloaddition reaction in the supramolecular (***S***)-**16a** solution to be faster than in the monomeric solution. This finding opens new avenues for obtaining photoresponsive chiral optoelectronic devices from light-controlled supramolecular systems.

In the design of π-conjugated systems exhibiting CPL activity, it is important to consider the restriction of intramolecular motions. In any case, this restriction of intramolecular rotation can promote a staggered arrangement of the monomer, leading to the formation of *J*-type supramolecular polymers with enhanced emission dissymmetry factor and quantum yield, as seen in the chiral anthraquinone-based compounds (***S***)-**17a** and (***S***)-**18** (Fig. 13a).[26] In both compounds, amide groups promote supramolecular polymerization through hydrogen bonding and π-stacking interactions. However, in (***S***)-**17a**, the inclusion of an acetylene spacer enforces an almost coplanar geometry between the anthraquinone and phenyl units with a torsion angle of 1.81°, thus favoring efficient slipped *J*-aggregation. This optimized packing facilitates effective chirality transfer from the stereocenters to the emissive core and induces a significant change in the emission pathway from cyan fluorescence in the monomeric state to yellow phosphorescence in the polymeric form, with the emission lifetime increasing 71-fold. The quantum yields improved sevenfold, and $g_{lum}$ reached 0.031 with a high CPL brightness value of 13.8 $M^{-1}$ $cm^{-1}$, which exceeds the typical detection threshold for point-chiral organic luminophores (Fig. 13b and c). This improvement is also evident in the formation of long-range-ordered 1D nanofibers with a length of a few micrometers and an average height of 4.7 nm, as observed by AFM. Conversely, (***S***)-**18**, which lacks acetylene linkers, exhibits a significantly twisted conformation with an angle about 33.4°. This distortion disrupts *J*-aggregation, leading to complete quenching of CPL activity with the formation of nanoparticles, as observed in the AFM images. Additionally, Förster resonance energy transfer (FRET) was introduced by doping (***S***)-**17a** assemblies with the red-emissive acceptor **19**.

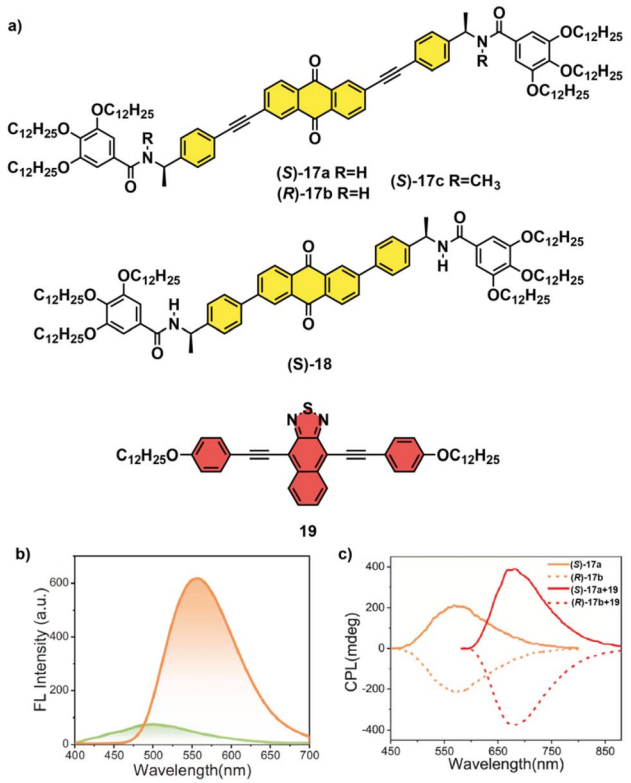


Fig. 13 (a) Chemical structures of compounds (*S*)-17a and b, control compounds (*S*)-17c and 18, and energy acceptor 19; (b) emission spectra of (*S*)-17a in chloroform (green line) and MCH (orange line) upon excitation at 365 nm; and (c) CPL spectra of supramolecular polymeric films of (*S*)-17a, (*R*)-17b and binary complex (*S*)-17a + 19 or (*R*)-17b + 19 upon excitation at 365 nm. (Reproduced from ref. 26 with permission from Wiley-VCH, Copyright 2025).

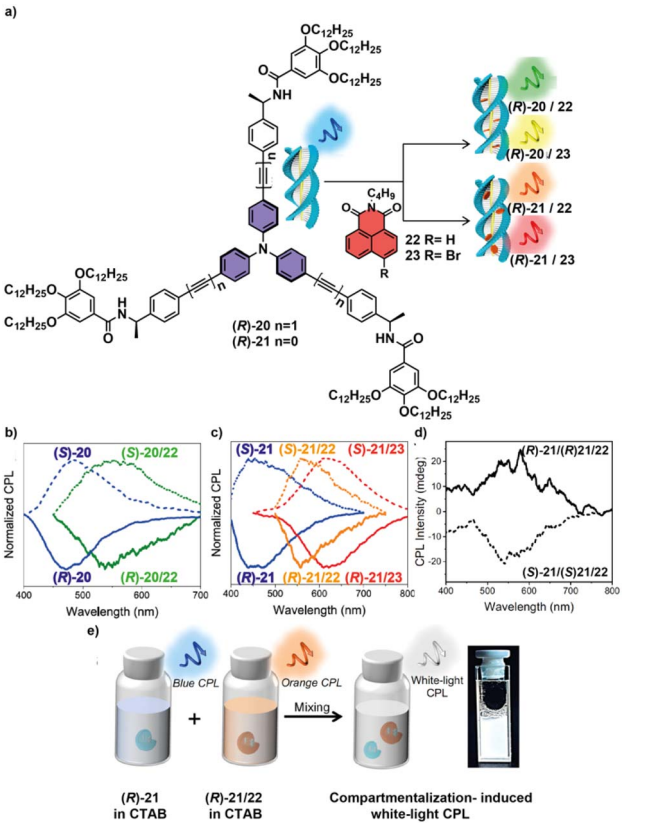


Fig. 14 (a) Chemical structures of triphenylamine donor compounds (*R*)-20 and (*R*)-21, naphthalenemonoimide acceptor compounds 22 and 23 and schematic of wide-range tuneable circularly polarized luminescence of supramolecular donor–acceptor polymers *via* intermolecular charge-transfer complexation. (b and c) Normalized CPL spectra of supramolecular donor polymers 20 and supramolecular donor–acceptor polymers 20/22 in the film state (b) and 21, together with supramolecular donor–acceptor polymers 21/22 and 21/23 in the film state upon excitation at 365 nm (c). (d) Mirror-image CPL of white-light emissive (*R*)-21/22 and (*R*)-21/23 (solid line) and (*S*)-21/22 and (*S*)-21/23 (dotted line) aqueous solutions encapsulated in CTAB. (e) Schematic of the preparation of white-light luminescent (*R*)-21/22 encapsulated in CTAB. (Reproduced from ref. 27, CC BY-NC-ND).

This enables color-tunable CPL, shifting the emission from yellow to red while significantly boosting the efficiency (quantum yield up to 41.7%) and dissymmetry ($g_{lum} = 0.060$). Prototype CPL-emitting LED devices exhibited strong, stable CPL signals with excellent reversibility under electrical driving, confirming their potential for practical chiral optoelectronic applications.

Additionally, another interesting strategy reported by Wang *et al.* involved the incorporation of intermolecular charge-transfer complexation into chiral supramolecular polymers to achieve tuneable CPL.[27] Specifically, two enantiopure triphenylamine donors, (*R*)-20 and (*R*)-21, were synthesized. In one case, *N*-[(1*R*)-phenylethyl]benzamide units are incorporated at the peripheries of the triphenylamine core in (*R*)-20, while in (*R*)-21, these substituents lack the acetylene linkages, as illustrated in Fig. 14a. Both donors (*R*)-20 and (*R*)-21 self-assemble into helical supramolecular polymers through threefold hydrogen bonding *via* a cooperative nucleation–elongation mechanism, as confirmed by the temperature-dependent experiments. The only experimental difference between these two supramolecular polymers was that (*R*)-21 showed higher thermo-stability and stronger gelation tendency than (*R*)-20 under identical conditions. These phenomena were attributed to different twisting of their triphenylamine cores. The lack of acetylene linkages induces an increase in the rotation angle from 6.5° in trimeric species (*R*)-$20_3$ to 11.9° in (*R*)-$21_3$, resulting in strengthened hydrogen bonding with intermolecular N–H···O distances between adjacent amides of 1.85–18.9 Å in (*R*)-$20_3$ *versus* 1.82–1.86 Å in (*R*)-$21_3$, which was confirmed by DFT calculations. This finding aligns with the Gibbs free energy changes observed in the supramolecular polymerization process, indicating that (*R*)-21 is 2.3 kJ $mol^{-1}$ higher in energy compared to (*R*)-20. Moreover, supramolecular homopolymers of (*R*)-20 and (*R*)-21 displayed blue-coloured CPL with $g_{lum}$ values of $-7.2 \times 10^{-3}$ and $9.4 \times 10^{-3}$ at 472 and 453 nm (Fig. 14b and c), respectively.

At this point, the introduction of naphthalenemonoimide (NMI) acceptors (22 and 23) into the homopolymers allows the formation of a donor–acceptor complex. Here, modulation of the CT strength is achieved through adjustments to structural

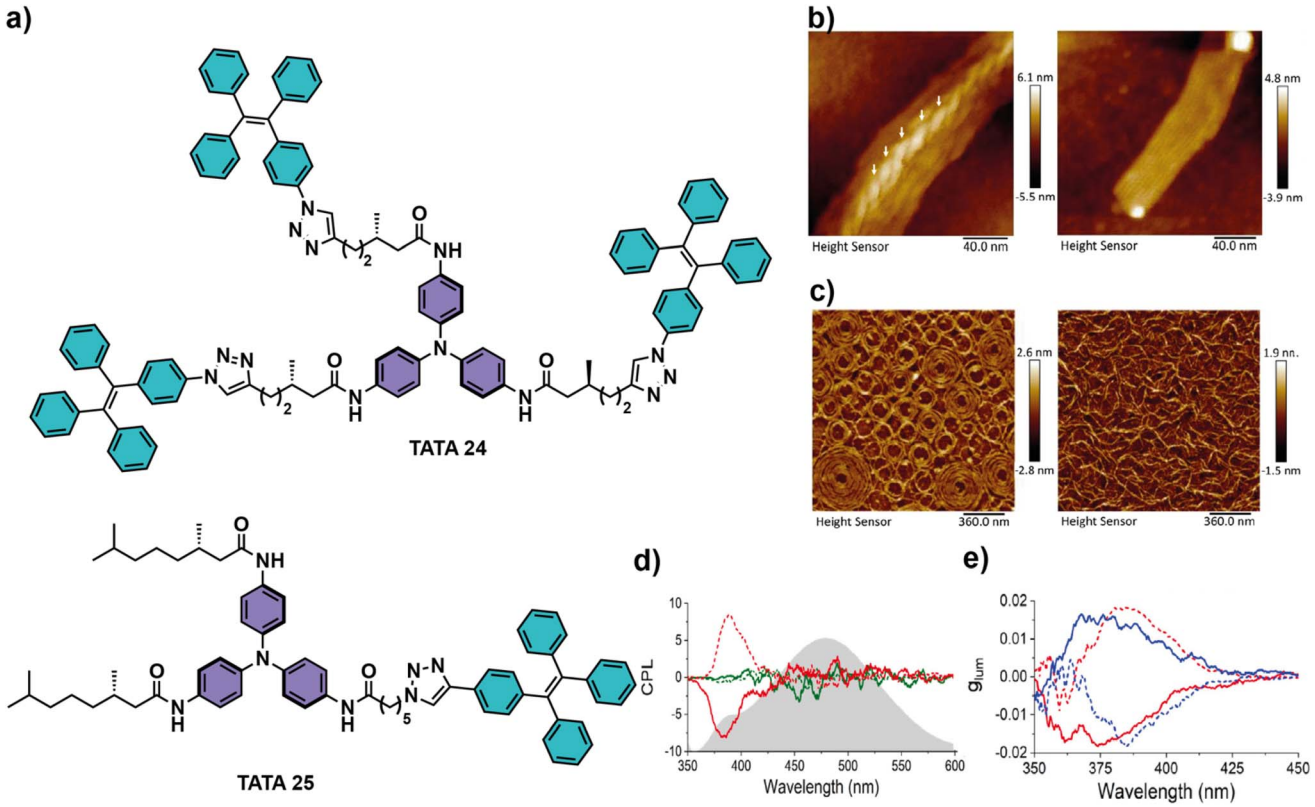


Fig. 15 (a) Structure of **TATA-24** and **TATA-25** monomers; (b) AFM micrographs of the self-assembled structures obtained upon fast cooling of **TATA-24** (left) and slow cooling (right); (c) **TATA-25**, fast cooling (left) and slow cooling (right); (d) CPL spectra of **TATA-24** (green) and **TATA-25** (red) obtained upon fast cooling (dashed line) and slow cooling (solid line) and emission spectra of **TATA-25** obtained upon slow cooling (grey area); (e) $g_{lum}$ values of **TATA-25**, red for the *S* enantiomer and blue for the *R* enantiomer, obtained upon fast cooling (dashed line) and slow cooling (solid lines) (reproduced from ref. 28, CC BY-NC-ND).

features such as the acetylene linkages on the triphenylamide donor, which modify the HOMO energy levels, or bromination on NMI, which alter the LUMO energy levels, providing supramolecular donor–acceptor polymers with tuneable CPL signals. These CPL signals vary from green and yellow for supramolecular donor–acceptor polymers **(*R*)-20/22** and **(*R*)-20/23**, to orange and red for **(*R*)-21/22** and **(*R*)-21/23** (Fig. 14b and c), respectively. These subtle structural variations dictate the donor–acceptor packing modes, which, in turn, control the ground-state *versus* excited-state CT pathways, resulting in distinct emission wavelengths and lifetimes. This study further resolved challenges in achieving white-light CPL by employing surfactant-based micellar compartmentalization, allowing blue-emitting TPA polymers and orange-emitting CT complexes to coexist without mutual quenching (Fig. 14d and e). Overall, this work demonstrates that precise manipulation of CT interactions within chiral supramolecular polymers provides a robust and modular approach for designing CPL-active materials with full-spectrum tunability, suitable for advanced photonic and display technologies.

Giuseppone, Bassani and Moulin proposed the first supramolecular polymer in which the handedness of the emitted circularly polarized light can be switched using the same enantiopure building block by merely adjusting the cooling speed during self-assembly.[28] This effect has been attained by the self-assembly of the two chiral triarylamine-based monomers **TATA-24** and **TATA-25** (Fig. 15). In the first one, $C_3$-symmetric **TATA-24**, three tetraphenylethene (TPE) fluorophores units are connected to the TATA core through three linkers containing (*S*) stereocenters based on citronellol. In the second monomer, **TATA-25**, a single TPE unit is linked to the TATA core through an achiral chain, while the chirality of the self-assembly is directed by two additional chiral side arms. They first examined the self-assembly behaviour of both monomers by controlling the cooling of their chlorobenzene solutions using two different protocols: fast cooling, in which a hot solution is cooled directly to −20 °C, and slow cooling, where the temperature is reduced at a controlled rate of 0.5 °C $min^{-1}$ or slower. Using AFM and TEM imaging, these authors observed that the **TATA-24** monomer formed thick, bundled fibrillar aggregates under rapid cooling. These structures consisted of irregular fibers with a diameter of 7–10 nm, intertwined into *M*-type superhelical domains (Fig. 15b). In contrast, slow-cooling produced straight, more ordered flat ribbons with widths ranging from 10–50 nm and a uniform height of 2 nm, composed of parallel fibrils spaced about 3 nm apart (Fig. 15b).

On the other hand, the **TATA-25** monomer upon fast-cooling produced flat, circular objects with heights of 2 nm, composed

of loosely aggregated single fibrils exhibiting P-type helicity. In contrast, when this sample was slowly cooled, it formed twisted fibers that further intertwined into larger, diffuse microgel networks (Fig. 15c). These fibers display twisted segments characteristic of M-type superhelical arrangements, generated by the coiling of 2–3 single fibrils. These distinct structures arise from the competition between primary nucleation growth under fast cooling and secondary nucleation/elongation growth under slow cooling. In addition, chiroptical and spectroscopic properties were studied for both monomers, which also showed differences between the two cooling regimes. The absorption spectra exhibited a blue shift in the aggregate state of the **TATA-24** and **TATA-25** monomers compared with the monomers in the dissolved state, confirming the formation of H-type aggregates. The slow-cooled samples exhibited weaker absorption intensities than the fast-cooled ones, indicating stronger electronic interactions between the TATA units in the former self-assembled structures. CD experiments revealed bisignate CD signals, with opposite signs under fast and slow cooling, which matched the helicities observed *via* AFM. It is noteworthy that the CD intensities for **TATA-25** were stronger than those for **TATA-24**, suggesting better chromophore organization. This tendency was also observed in the emission spectra. **TATA-24** and **TATA-25** displayed AIE due to the presence of TPE; however, **TATA-25** emitted more intensely despite having fewer TPE units, showing that supramolecular packing dominates emission behaviour. Finally, the ability of self-assemblies to emit circularly polarised light was investigated. While no CPL signal was observed for **TATA-24**, **TATA-25** showed strong CPL signals of opposite handedness depending on the cooling conditions, which originated from the TATA locally excited state (Fig. 15d and e). For each enantiomer, the fast and slow-cooled samples showed circularly polarized emission of similar intensities, with maximum recorded $g_{lum}$ values of $+1.8 \times 10^{-2}$ and $-1.7 \times x$ $10^{-2}$ for the (*S*) enantiomer, and $-1.8 \times 10^{-2}$ and $+1.5 \times 10^{-2}$ for the (*R*) enantiomer, respectively, falling within the range of the highest reported values for supramolecular systems in solution. These findings demonstrate that circularly polarized light of either handedness can be produced from the same enantiomer simply by controlling the temperature during its self-assembly process, a capability that stems from the hierarchical organization of the TATA core. This work introduces a new strategy for designing optically active materials, enabling precise control of CPL without altering molecular chirality-only assembly conditions.

An important challenge in the development of supramolecular polymers exhibiting CPL activity is the attainment of reproducible and highly controlled structural parameters, including dimensional precision and low dispersity, as they govern the properties of the resulting materials. Furthermore, achieving this level of control in an aqueous medium would significantly broaden the scope of chiroptical applications, particularly within biologically relevant environments. In this regard, to precisely control the length and dispersity of supramolecular polymers with CPL activity in water, the use of living supramolecular polymerization (LSP) was proposed by George and coworkers.[29] They designed two ethoxy-core-substituted naphthalene diimide (cNDI) molecules appended with a chiral dipeptide, denoted as *L*-**26** and *D*-**26**, respectively (Fig. 16a). These monomers interact *via* π-stacking between the cNDI units, while the chiral peptide side chains promote intermolecular hydrogen bonding through their amide groups, leading

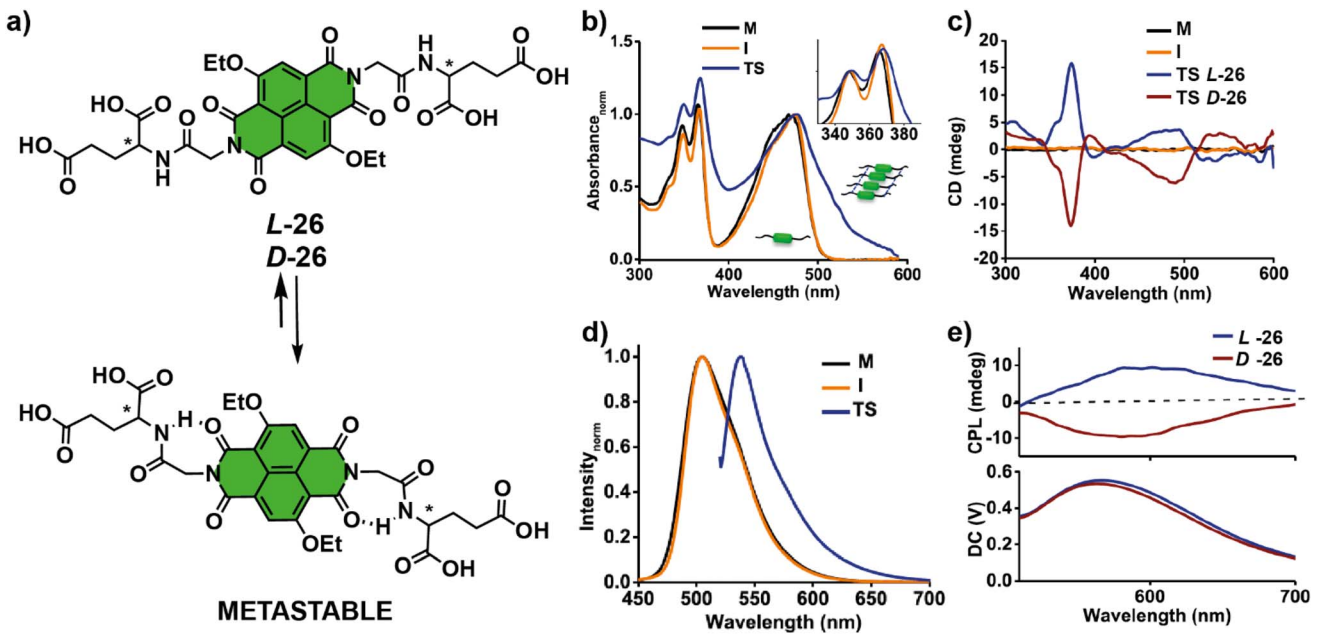


Fig. 16 (a) Structure of *L*-26 and *D*-26 monomers. Comparison of (b) normalized absorption (inset corresponds to zoomed-in normalized absorption spectra at 346 nm); (c) CD spectra (thermodynamically stable state, TS, of both *L* and *D* isomers); (d) normalized emission for monomer (M), metastable (I) and TS showing distinct signals; and (e) CPL and corresponding DC spectra of *L*-26 and *D*-26. (Reproduced from ref. 29 with permission from Wiley-VCH, Copyright 2021).

to the formation of extended supramolecular polymers and imparting chirality to the cNDI core during self-assembly. Additionally, the carboxylic acid groups engage in hydrogen bonding with water, enabling supramolecular polymerization in aqueous media. By exploiting pathway complexity, where monomers pass through monomeric (M), metastable (I), and thermodynamically stable (TS) states, the authors achieved kinetically controlled nucleation–elongation behaviour. Through temperature-dependent spectroscopy measurements, the monomer, metastable and thermodynamically states were fully characterized. A sharp vibronic feature in the absorption bands, absence of a CD signal, and a narrow emission at 505 nm were observed for the monomer of *L*-**26**. Upon fast-cooling, a slight red shift in the absorption bands with an increased ratio between the vibronic bands at 365 and 346 nm with the persistent absence of a CD signal, and insignificant change in the emission and excitation spectra suggested the presence of small aggregates, which were identified as metastable states (Fig. 16b–d). The time-dependent absorption spectra exhibited a gradual red shift and broadening of the absorption band, accompanied by the appearance of a new absorption at *ca.* 510 nm. These changes indicate the evolution toward a thermodynamically stable self-assembled state by the dynamic reorganization of the monomers from their metastable phase (I) through extended intermolecular hydrogen bonding. This was also confirmed by the bisignate CD spectrum centered at the π–π* and n–π* bands of cNDI, accompanied by the appearance of a new characteristic band at *ca* 538 nm, as shown in Fig. 16c. The resulting supramolecular polymers showed a strong chiroptical performance, with a notable CPL dissymmetry factor of $1.3 \times 10^{-3}$ (Fig. 16d). Moreover, seeding strategies varying the seed concentration, monomer concentration and seed fragmentation *via* sonication were used to bypass nucleation and achieve highly efficient seeded growth, producing fibers with precisely tuneable lengths and very low dispersity. Multicycle seeding resulted in living behaviour, enabling stepwise, length-controlled elongation. Overall, this work demonstrated one of the most efficient aqueous-phase LSP systems reported in the literature, illustrating how LSP can be used to create functionally active, CPL-emitting supramolecular polymers with programmable structure-opening pathways for biological and optoelectronic applications.

## Axial chirality in CPL-active supramolecular polymers

In the last few sections, we have seen that helical supramolecular polymers formed by the self-assembly of chiral scaffolds endowed with peripheral side chains decorated with stereogenic centres behave as CPL-active materials. However, in most of the reported examples of these chiral, CPL-active supramolecular polymers, their $g_{lum}$ values are moderate. Given that a major challenge faced by researchers in this field is to enhance the anisotropic $g_{lum}$ factor, a valuable strategy involves utilizing chiral scaffolds in which asymmetry is present in the chromophore instead at the peripheral side chains. This strategy involves the self-assembly of chiral units exhibiting axial chirality, *i.e.*, asymmetry stemming from a chiral axis instead of a central carbon atom. Relevant examples of CPL-active supramolecular polymers in which the central aromatic core is endowed with helicenes, binaphthyls or *p*-cyclophanes have been reported in the bibliography, exhibiting remarkable anisotropy factors. In this section, we review some of the most significant reports related to this strategy.

Although helicenes, as ortho-fused aromatic compounds that yield helical chirality,[30] have been extensively reported as efficient CPL-active systems,[31] much less studies have been published on CPL-active, helicene-based supramolecular polymers. Probably, one of the first examples of CPL-active SPs was phthalhydrazide-functionalized [7]helicene **27** reported by Takeuchi and coworkers in 2011 (Fig. 17a). The two (*M*) and (*P*) enantiomers of **27** were separated by column chromatography on a chiral support. Enantioenriched (*M*)-[7]helicene **27** forms trimeric disks *via* intermolecular H-bonding interactions between the phthalhydrazide units. These disks, due to the π-stacking of the [7]helicene cores, yield screw-shaped fibrous assemblies in toluene as the solvent (Fig. 17b). The SPs formed by the self-assembly of the enantioenriched *M* and *P* enantiomers displayed mirror-image CPL spectra with outstanding $g_{lum}$ values of 0.035 at the peak maxima.[32]

[5]Helicenes, decorated with two methyl groups at the 1 and 1′ positions to prevent racemization of their aromatic core and with imide units, have been reported to self-assemble into

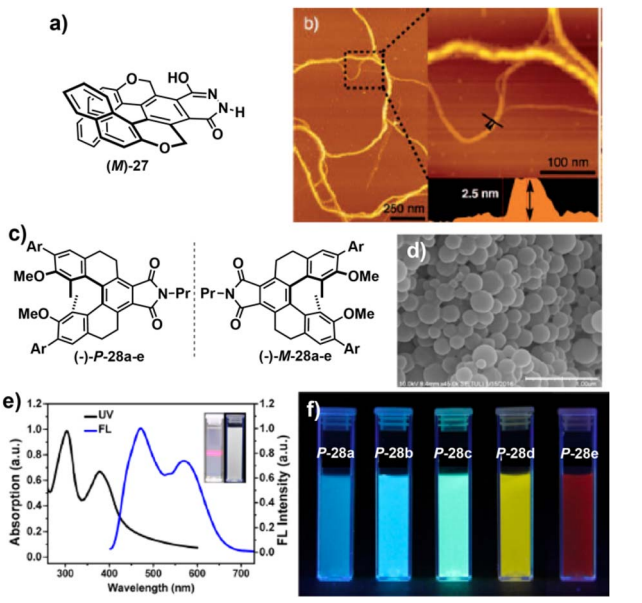


Fig. 17 (a) Chemical structure of phthalhydrazide-functionalized [7]helicene **27** and (b) AFM images of (*M*)-**27** prepared in toluene (reproduced from ref. 30 with permission from Wiley-VCH, Copyright 2011). (c) Chemical structure of the *P* and *M* enantiomers of tetrahydro [5]helicenes **28** and SEM image (d) and UV-vis and fluorescence spectra (e) of the nanoparticles formed by the co-assembly of (+)-*M*-**28a**, **28d**, and **28e** in water. The inset photographs in panel (e) are images of the nanoparticles observed by the naked eye and under 365 nm UV light. (f) Dispersion colours of the nanoparticles formed by [5]helicenes **28** under 365 nm excitation (panels 2 d–f reproduced from ref. 33 with permission from the American Chemical Society, Copyright 2018).

luminescent, spherical and uniform nanoparticles with a diameter of 200 nm upon injecting a THF solution of *M*- or *P*-enantioenriched tetrahydro[5]helicenes **28** into a water solution. [5]Helicenes **28** present different aryl groups at the 3 and 3′ positions, allowing modulation of their emission colour (Fig. 17). Interestingly, the co-assembly of [5]helicenes **(+)-*M*-28a**, **28d**, and **28e**, each emitting separately in the blue, green and red region, respectively, affords white-emitting nanoparticles (Fig. 17d and e).[33]

[6]Helicenes are well-known scaffolds exhibiting not only exciting CPL-activity with outstanding $g_{lum}$ values but also high $B_{CPL}$ values.[6b,34] Importantly, unlike [5]helicenes, [6]helicenes possess a high racemization barrier, making it unnecessary to decorate the bay position of the helicene core to prevent racemization of the corresponding *M* and *P* enantiomers of these helicenes.[30] We reported on the formation of chiral SPs using 2,15- and 4,13-disubstituted [6]helicenes endowed with peripheral benzamide units (compounds **29-32**, as shown in Fig. 18a).[35] We demonstrated that these series of [6]helicenes are molecularly dissolved in good solvents such as chloroform but in non-polar solvents such as MCH, they readily form chiral supramolecular polymers with rich chiroptical features. Interestingly, the substitution pattern of the [6]helicene core plays a crucial role in the self-assembling mode of the monomeric units and, consequently, in the chiroptical features. Thus, in 2,15-disubstituted [6]helicenes **29** and **31**, the central aromatic core is not available for π-stacking of the monomeric units, and intermolecular H-bonding interactions between the amide functional groups of the peripheral side chains result in a zigzag arrangement of the chromophores (Fig. 18b). On the contrary, in 4,13-disubstituted [6]helicenes **30** and **32**, the central aromatic cores are more available for π-stacking, and the resulting SPs are formed by the synergy of both intermolecular H-bonding interactions between the amide functional groups and the π-stacking of the aromatic backbones. The synergy of these non-covalent interactions results in a ladder-like arrangement of the monomeric units to give rise to the corresponding chiral supramolecular polymer (Fig. 18b). To evaluate the stability of the supramolecular polymers formed by **29** and **30**, solvent denaturation (SD) experiments were performed using mixtures of these helicenes in chloroform, a good solvent that induces the disassembly of the SP, and in MCH, a poor solvent favouring self-assembly.[36] Interestingly, the substitution pattern of the [6]helicene core plays a relevant role in the supramolecular polymerization mechanism of these two systems. Thus, whilst 2,15-disubstituted helicene **29** follows an isodesmic supramolecular polymerization mechanism, 4,13-disubstituted helicene **30** is governed by a cooperative mechanism. The emission spectra of both enantiomers, *M* and *P*, of [6]helicene **29** in $CHCl_3$ show the characteristic vibronic structured photoluminescence (PL) of [6]helicenes[31] with three consecutive maxima at 430, 455, and 486 nm ($\lambda_{exc} = 365$ nm, $\phi = 0.35$, and $\tau = 8.5$ ns) (Fig. 18d). This vibronic structure is also observed in the corresponding CPL spectrum, which exhibits a remarkable dissymmetry factor ($g_{lum}$) with maximum values of $+2.3/-2.6 \times 10^{-2}$ ($\lambda_{exc} = 365$ nm) for **(*P*)-29** and **(*M*)-29**, respectively (Fig. 18d). The emissive properties of the supramolecular polymers formed by these enantiomers in MCH also display very similar, but slightly red-shifted features with maxima at 436, 462, and 493 ($\lambda_{exc} = 365$ nm, $\phi = 0.59$, and $\tau =$

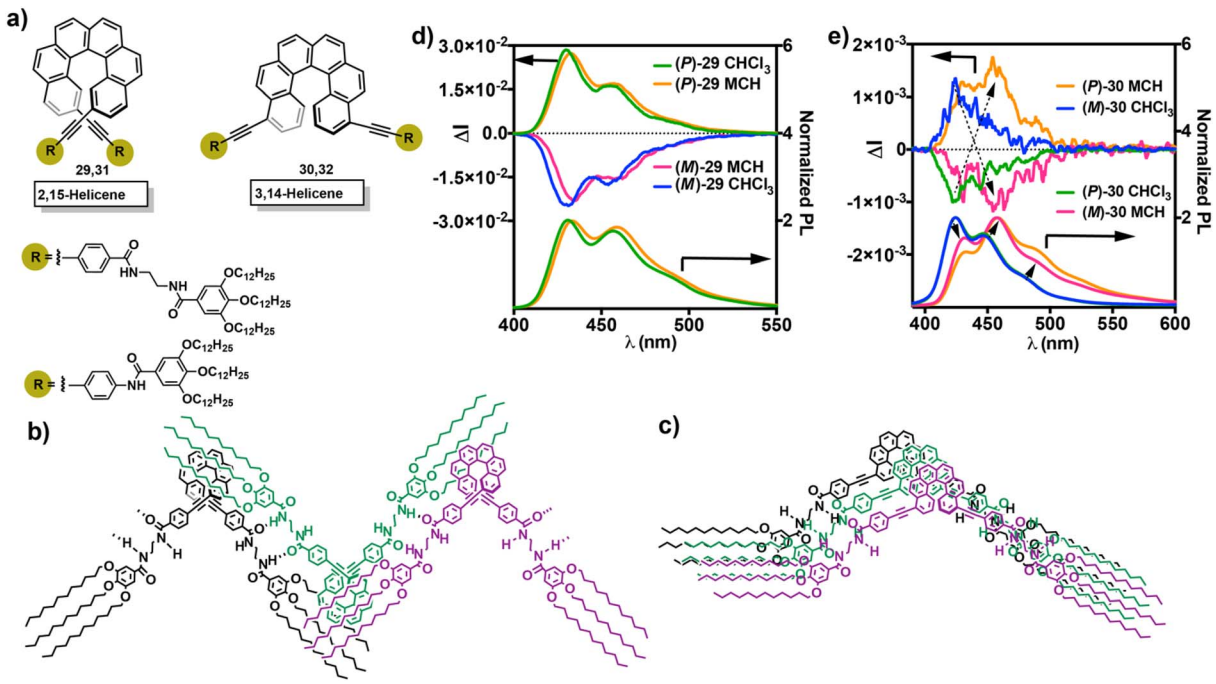


Fig. 18 (a) Chemical structure of [6]helicenes **29-32**; (b) and (c) schematic of the binding mode experienced by [6]helicenes **29**, **31** (b) and **32** (c) upon self-assembly; and CPL/PL spectra of **(*P*)-29** and **(*M*)-29** (d) and **(*P*)-30** and **(*M*)-30** (e) in monomeric and aggregated states ($CHCl_3$ and MCH, respectively). (Reproduced from ref. 35 with permission from the American Chemical Society, Copyright 2022).

12.2 ns). These maxima are also observed in the CPL spectra with maximum $g_{lum}$ values of +2.0/−2.3 × $10^{-2}$ ($\lambda_{exc}$ = 365 nm), respectively. These results demonstrate that the lack of π-stacking in the self-assembly of [6]helicenes **29** results in analogous values for the CPL activity of both the aggregated and non-aggregated states.[35a]

As in the previous example, the fluorescence spectra of **(*P*)-30** and **(*M*)-30** in $CHCl_3$ and MCH display vibronic-structured luminescence with the characteristic three consecutive maxima at around 430, 455 and 485 nm (Fig. 18e). The substitution pattern of these [6]helicenes **30** plays a relevant role decreasing the $g_{lum}$ values of both the monomeric species (−1.1/+1.3 × $10^{-3}$ for the *M* and *P* enantiomers, respectively, in $CHCl_3$, Fig. 18e) and aggregated species (+1.4/−1.2 × $10^{-3}$, for the *P* and *M* enantiomers, respectively, in MCH; Fig. 18e). To the best of our knowledge, this is the first observation of CPL sign inversion upon assembly in helicenes.[35a]

The presence of only one amide functional group per branch in [6]helicenes **31** and **32** notably reduces the stability of the aggregated species formed by these helicenes. However, the 2,15- and 4,13-substitution patterns result in a similar zigzag and ladder-like arrangement of the monomeric units in the corresponding aggregated species formed by **31** and **32**, respectively. In these helicenes, the CPL activity of both monomeric and aggregated species is very similar to those recorded for compounds **29** and **30** with $g_{lum}$ values of +2.8/− 2.6 × $10^{-2}$ for **31** and +2.0/−2.0 × $10^{-3}$ for **32**. It is worth mentioning that in this case, and unlike to those observed for [6]helicene **30**, the CPL of both the monomeric and aggregated states of **32** display the same sign.[35b]

We have already seen that a common strategy to improve the emission of supramolecular polymers involves utilizing non-planar aromatic units, which, through AIE, result in an increase in emission intensity. This AIE phenomenon has been also utilized in CPL-active supramolecular polymers in which the monomeric species are decorated with point chirality in the peripheral side chains, as shown in the previous section.[22] With this idea in mind, the previously mentioned 2,15- and 4,13-disubstituted [6]helicene cores were functionalized with cyanostilbene moieties (compounds **33**, Fig. 19a). The resulting [6]helicene monomeric species readily form chiral supramolecular polymers in non-polar MCH following a cooperative mechanism, regardless of the substitution pattern. Despite the clear increase in the emission intensity upon aggregation (Fig. 19b and c), the CPL activity of the corresponding chiral supramolecular polymers of **33** is similar to that observed for [6]helicenes **30** and **32** with $g_{lum}$ values of around +2/−2 × $10^{-3}$ for each enantiomer (Fig. 19d and e), respectively.

The presence of cyanostilbene moieties in 2,15-disubstituted [6]helicene **33a** result in lower $g_{lum}$ values than that reported for [6]helicenes **29** and **31** (Fig. 19d and e).[37] Despite their relatively low $g_{lum}$ values, the remarkable AIE observed upon self-assembly results in enhanced $B_{CPL}$ values. This parameter increases from 2.8 and 5.4 for the monomeric species to 11.6 and 40.6 for **33a** and **33b**, respectively.[37] The restricted rotation around the single bond connecting two aromatic rings makes biaryl-based compounds excellent chiral scaffolds for inducing

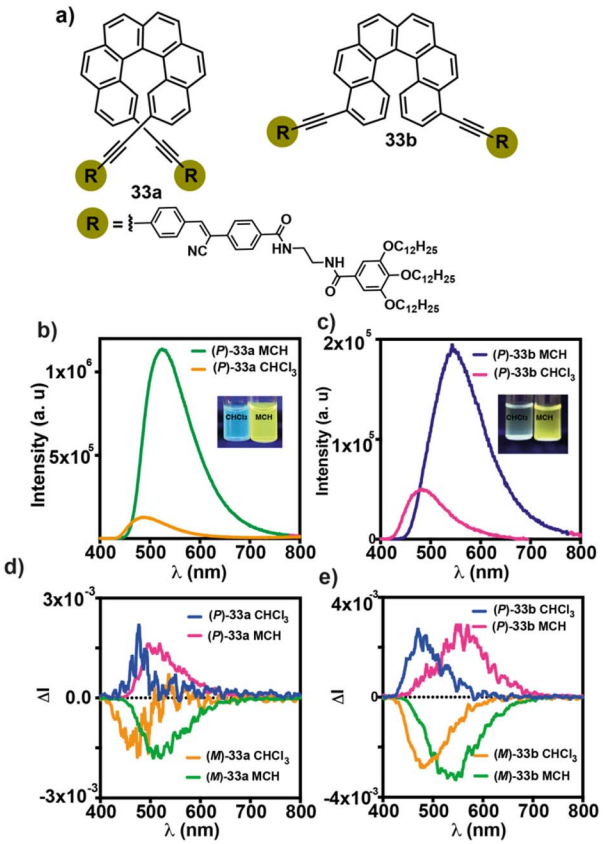


Fig. 19 (a) Chemical structure of [6]helicenes **33**; emission spectra of **(*M*)-33a** (b) and **(*M*)-33b** (c); and CPL spectra of **(*M*)-33a** and **(*P*)-33a** (d) and **(*M*)-33b** and **(*P*)-33b** (e) in $CHCl_3$ and MCH, respectively. The inset in panels (b) and (c) show pictures of solutions of **(*M*)-33a** (b) and **(*M*)-33b** (c) in $CHCl_3$ and MCH upon excitation at λ = 365 nm. (Reproduced from ref. 37 with permission from the Royal Society of Chemistry, Copyright 2024).

stereoselectivity in various applications and, additionally, to achieve CPL-active systems.[38,39]

Enantioenriched biaryl-based compounds have been also utilized as monomeric units to attain chiral supramolecular polymers displaying different CPL activity for aggregated species than that registered for the monomeric species. To the best of our knowledge, one of the first examples of CPL-active supramolecular polymers possessing biaryl units was reported by Kumar, Nakashima, Tsumatori and Kawai in 2014. In these CPL-active supramolecular polymers (compounds **34**, as shown in Fig. 20a), an enantioenriched binaphthalene core, *R or S*, was decorated with two asymmetrically substituted perylenediimide (PDIs) units, a highly utilized chromophore to prepare supramolecular polymers with exciting optical and chiroptical properties,[40] which self-assemble into nanoparticles or 1D supramolecular polymers depending on the concentration range or the solvent utilized to form the corresponding supramolecular ensembles (Fig. 20a). The presence of a chiral binaphthalene core in compounds **34** results in a clear chiroptical response for the molecularly dissolved monomeric species in $CHCl_3$ with a total concentration of 10 μM, exhibiting $g_{lum}$ of

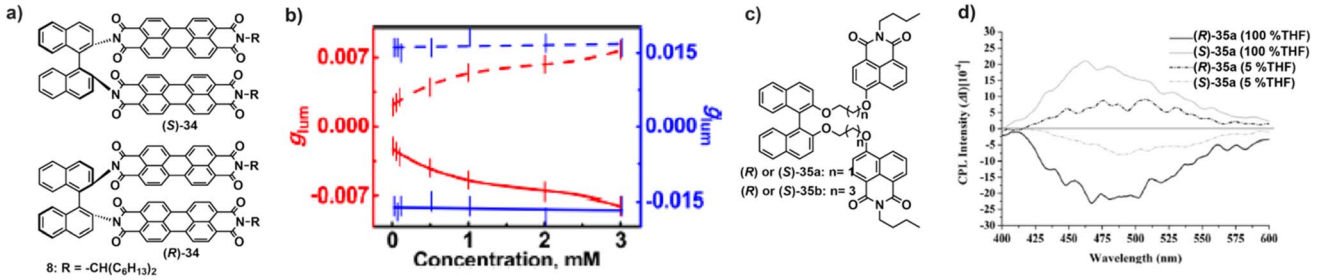


Fig. 20 (a) Chemical structure of binaphthalene derivatives **34** and (b) plot of $g_{lum}$ *vs.* concentration for *R* (solid lines) and *S* (broken lines) enantiomers of **34** in $CHCl_3$ (red traces) and a mixture (1 : 19) of $CHCl_3$/MCH (blue traces). (Reproduced from ref. 41 with permission from the American Chemical Society, Copyright 2014.) (c) Chemical structure of chiral monoimides **35** and (d) CPL spectra of **35a** in THF and 5 : 95 (v/v) THF/$H_2O$ mixtures. (Reproduced from ref. 43 with permission from Wiley-VCH, Copyright 2015).

~0.003. Increasing the concentration of these chromophores to 3 mM in $CHCl_3$ yielded uniform nanoparticles with a diameter of 26 nm and $g_{lum}$ values up to 0.008, implying the contribution of the chiral aggregates to the enhanced fluorescence dissymmetry. On the other hand, using a mixture of MCH/$CHCl_3$ (19 : 1) as the solvent induced efficient supramolecular polymerization of these PDI-based systems **34**, which yielded H-type aggregates showing a rope-like morphology. Furthermore, a noticeable increase in the $g_{lum}$ value to 0.018 was observed. It is worth mentioning that in this solvent mixture, unlike that observed in $CHCl_3$, the $g_{lum}$ values remain unaltered upon increasing the concentration (Fig. 20b).[41] Shortly after these studies, the authors performed a majority rules experiment in which both enantiomers, **(*S*)-34** and **(*R*)-34**, were mixed at different ratios but keeping the total concentration constant. These NMR experiments demonstrate that the morphology of the aggregates range from nanoparticles for a racemic mixture of both enantiomers to fibrillar supramolecular polymers. Furthermore, the $g_{lum}$ values were cancelled for the racemic mixture but increased to 0.02 when one of the enantiomers was in excess in the mixture.[42]

The decoration of enantioenriched binaphthalene cores with luminescent monoimides was reported by Zhang, Zhu, Cheng and coworkers to invert the CPL activity of the resulting chiral, luminescent systems **35** when the monomeric species self-assemble upon adding increasing amounts of water (Fig. 20c). The studies performed with these chiral monoimides demonstrate that the CPL activity is barely modified upon increasing the tether connecting both the binaphthalene and the monoamide units. However, the addition of water induces a clear increase in the $g_{lum}$ value due to the formation of aggregated species, in which the dihedral angle of the binaphthalene core decreases upon aggregation (Fig. 20d).[43] A similar strategy was employed by Balasubramanian, George and coworkers to achieve tuneable excimeric CPL spanning the visible range, with remarkable $g_{lum}$ values in the range of 0.015. These $g_{lum}$ values were obtained upon self-assembly of a chiral binaphthalene decorated with two naphthalenediimides (NDIs) **36**, which, in turn, were modified by attaching two electron-donating ethoxy groups. Whilst the monomeric species do not exhibit any CPL activity, the aggregates formed in mixtures of tetrachloroethane (TCE) and MCH show intense CPL activity and CPL brightness (Fig. 21a).[44]

The synergy of the asymmetry of a binaphthalene core, the ability of an anthracene moiety to self-assemble, and the narrow-band emissive properties of BODIPY has been harnessed to prepare CPL-active monomeric scaffold **37**. This scaffold self-assembles in a THF/$H_2O$ mixture, giving rise initially to an AIE phenomenon, which undergoes a light-triggered transition, yielding aggregation-caused quenching (ACQ) with a high $g_{lum}$ value of 0.048, one of the highest values

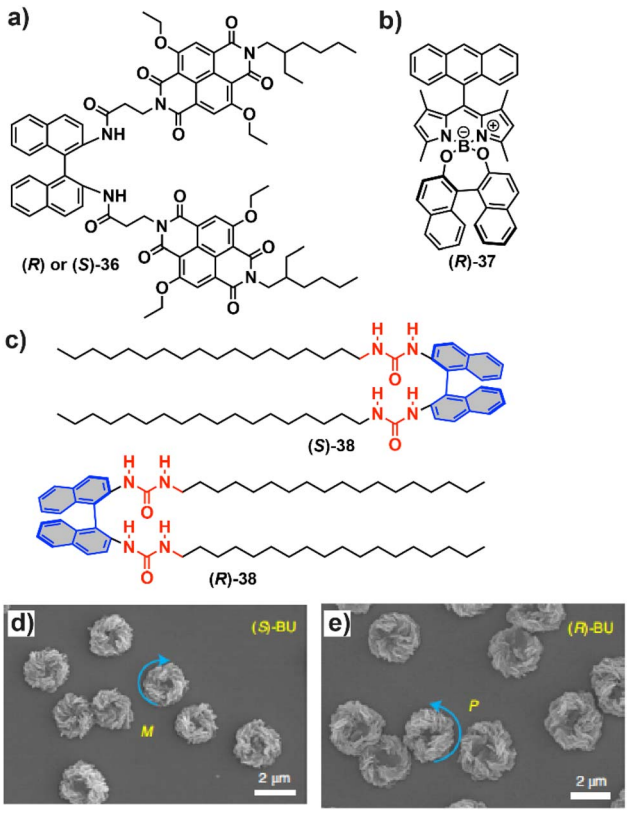


Fig. 21 Chemical structure of binaphthalene derivatives **36** (a), **37** (b) and **38** (c); and SEM images of the chiral toroids formed upon self-assembly of **(*S*)-38** (d) and **(*R*)-38** (e). (Reproduced from ref. 46 CC BY-NC-ND with permission from Springer, Copyright 2012).

reported for CPL-active supramolecular polymers (Fig. 21b).[45] The decoration of chiral binaphthalenes with urea moieties allowed Ouyang, Liu and coworkers to prepare helical toroids upon the hierarchical self-assembly of chiral compounds **38** (Fig. 21c). A drop-evaporation assembly protocol on a solid substrate from pre-assembled intermediate colloids of enantioenriched binaphthalene bisurea **38** led to microtoroids with preferred helicity due to the formation of H-bonds between the ureas and the π-stacking of the binaphthalene units (Fig. 21d and e). The molecular asymmetry embedded in the starting binaphthalenes conditions the final chirality of the toroidal aggregates. The chiral nature of these toroids results in a rich chiroptical response and the formation of CPL-active systems with $g_{lum}$ values of 0.002.[46]

The self-assembly of chiral scaffolds to yield supramolecular polymers is often accompanied by the formation of excimers, which can diminish the CPL activity of the aggregated species due to luminescence quenching. Thus, an effective strategy to cancel the excimer emission and increase the CPL activity involves the formation of charge-transfer (CT) complexes between chiral emissive arenes, acting as electron-donating segments, and different electron-withdrawing, achiral small molecules such as tetracyanobenzene (TCNB). In this case, the chiral, emissive, electron-donating system is based on a derivative of the (*S*)- or (*R*)-enantiomer of 5,5′,6,6′,7,7′,8,8′-octahydro-1,1′-binaphthalene endowed with pyrene (compound **39**, as shown in Fig. 22) or anthracene (compound **40**, as shown in Fig. 22). Whilst chiral **39** readily forms non-emissive CT-complexes with electron-withdrawing molecules such as tetrafluoro-*p*-benzoquinone, tetracyanoethylene or tetracyano-*p*-quinodimethane, the CT-complex formed by mixing **39** and TCNB results in a reddish, highly emissive species, which also presents a remarkable CPL activity, showing a $g_{lum}$ value of 0.017.[47] This strategy has been extended to octafluoronaphthalene (**OFN**). This electron-withdrawing system forms highly emissive CT-complexes with both chiral **39** and **40** due to the complementary arene–perfluoroarene interactions (Fig. 22). These emissive CT-complexes also present remarkable CPL activity with $g_{lum}$ values of $\sim 10^{-3}$, which are one-order of magnitude larger than that registered for the monomeric species.[48]

## Applications of CPL-active supramolecular polymers

In addition to the basic studies necessary to shed light on the achievement of efficient CPL-active supramolecular polymers, the most relevant issue for these materials is their application in different fields, especially in the fabrication of circularly polarized organic light-emitting diodes (CP-OLEDs) and sensing technologies. Upon reviewing basic aspects of CPL-active supramolecular polymers and the different families of compounds that show this relevant characteristic, this part of the review presents some of the applications reported in the literature regarding the fabrication of optoelectronic devices. Circular polarizers are widely employed in OLEDs to improve image contrast by reducing ambient reflectivity, but they attenuate nearly half of the emitted light, causing brightness loss and higher energy consumption. CP-OLEDs that emit circularly polarized light matching the handedness of the polarizer can avoid this inefficiency.[49] The first CP-OLEDs reported in the literature were fabricated by utilizing chiral, covalent polymers such as a chiral oligo(phenylenevinylene) or polyfluorene.[50] The incorporation of metal complexes such as Eu(III), Ir(III) or Pt(II) allows the fabrication of semitransparent devices with relatively high circularly polarized electroluminescence signals and high $g_{EL}$ up to −0.38 but still low efficiencies.[51] The incorporation of self-assembled structures has allowed better CP-OLED efficiencies to be achieved. Thus, Cheng and coworkers fabricated a device in which the active layer was prepared by combining chiral dihydropyridine **41a** and an achiral monoamide endowed with a triphenylamine moiety, **41b**, in which the former transfers its asymmetry to the latter and the resulting aggregates, upon annealing, present a strong CPL signal. The multisandwich device prepared from the helical aggregates generated upon mixing both **41a** and **41b**

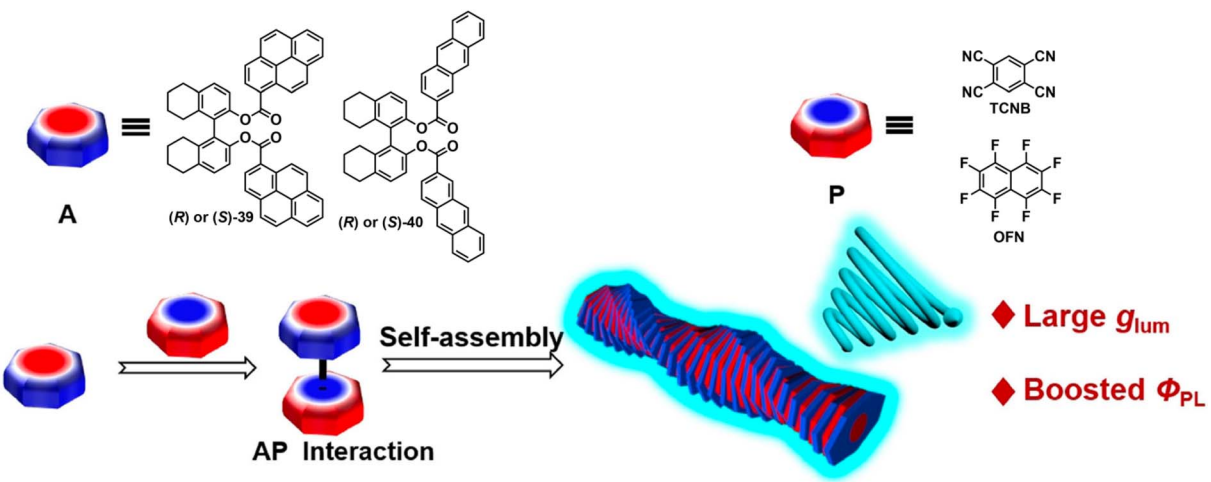


Fig. 22 Arene-perfluoroarene interactions between chiral π donors **39** or **40** and achiral π acceptors TCNB or OFN. (Reproduced from ref. 48 with permission from Wiley-VCH, Copyright 2021).

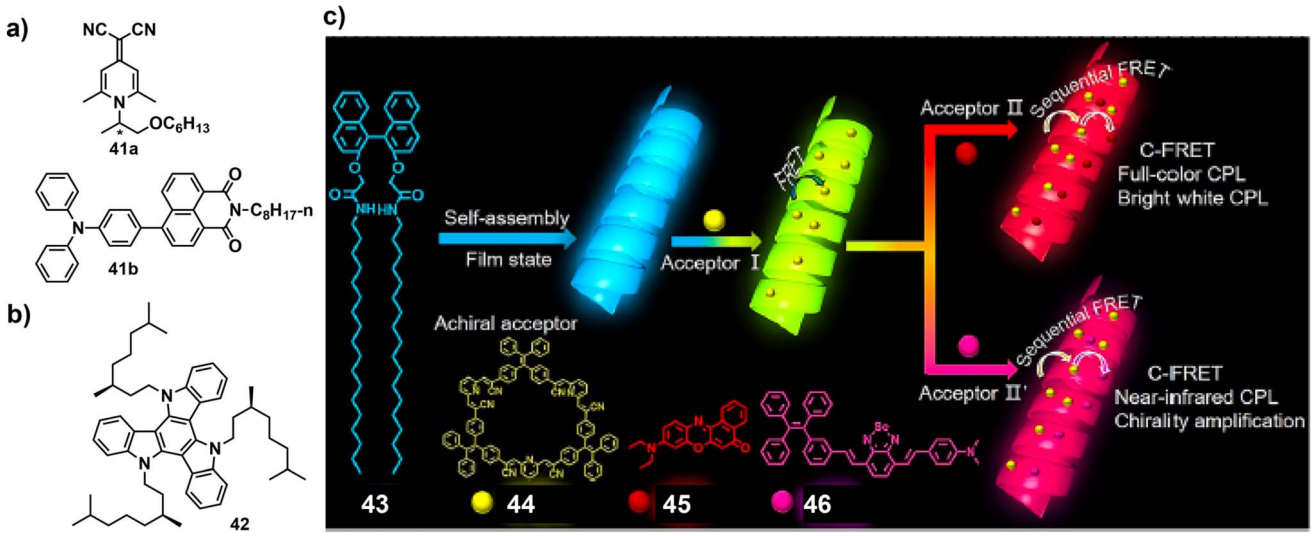


Fig. 23 Chemical structure of dihydropyridine **41a**, monoamide **41b** (a) and triazatruxene **42** (b). (c) Schematic of the process of chiral light harvesting and full-colour circularly polarized luminescence. In this system, **43** functions as an initiator of chirality, **44** serves as a conveyor, and **45** and **46** are the terminal acceptors. (Reproduced from ref. 54 with permission from the American Chemical Society, Copyright 2022).

exhibited strong brightness, good luminous efficiency, and a high $g_{EL}$ value of 0.023 (Fig. 23a).[52] Very recently, Meijer, Friend and coworkers reported the fabrication of a CP-OLED utilizing chiral triazatruxene **42**, which self-assembles into helical aggregates (Fig. 23b). Cosublimation of **42** as a guest within a structurally mismatched host, constituted by a mixture of the hole transporting 4,4′-bis(*N*-carbazolyl)-1,1′-biphenyl or the ambipolar 3′,5′-di(carbazol-9-yl)-[1,1′-biphenyl]-3,5-dicarbonitrile, enabled the formation of thin films in which chiral crystallization occurred *in situ via* thermally induced nanophase segregation of the dopant and host, while maintaining film integrity. The resulting OLEDs exhibited external quantum efficiencies of up to 16%, electroluminescence dissymmetries ≥10% and $g_{EL}$ values of 0.1.[53]

Zang *et al.* developed a chiral light-harvesting system (CLHS) based on sequential circularly polarized fluorescence resonance energy transfer (C-FRET) by integrating a chiral, light-absorbing initiator (**43**) with TPE-based macrocycles (**44**) exhibiting AIE, along with red and near-infrared emissive dyes (**45**-**46**). This design enabled continuous chirality transmission and amplification in conjunction with efficient energy transfer. In this system, a pair of chiral binaphthalene **43**, capable of self-assembling into helical nanostructures, was employed as the primary donor. Supramolecular assembly facilitated the successful incorporation of three energy acceptors, **44**–**46**, into the helical framework, producing a CLHS with tuneable fluorescence colours and stepwise energy and chiral transfer. The resulting system exhibited a maximum $g_{lum}$ value of 0.035. Further studies revealed that efficient energy transfer was promoted by the close spatial proximity between the donors and acceptors and their substantial spectral overlap. Moreover, the rigid cavity of the green-emitting AIE macrocycle **44**, together with hierarchical host–guest interactions, enabled the chirality of supramolecular synthons **43** to be continuously transferred and even amplified in the otherwise achiral dye molecules **45** and **46**. By optimizing the component ratios, the authors achieved an energy transfer efficiency of up to 98.5%, a fluorescence quantum yield of 37%, a $g_{lum}$ value of 0.035, CPL with tuneable emission colours, and a CPL emission approaching CIE standard white light across a broad spectral range (360–800 nm) (Fig. 23e).[54]

Finally, conventional methods such as barcodes, watermarks, and QR codes have become easy to replicate, which makes advanced anticounterfeiting technologies necessary. Chiroptical anticounterfeiting has emerged as a promising next-generation solution due to its multiple emission characteristics, including intensity, wavelength, lifetime, and chirality. Central to this approach is the development of CPL systems with high $g_{lum}$ values. An exciting anticounterfeiting effect has been reported using CPL-active systems such as a luminescent spiropyran and $Zn^{2+}$ (ref. 55) or nematic liquid crystals and photoswitches based on diarylethenes.[56] These seminal reports have complemented with the anticounterfeiting effect described by Zhang, Qu, Liu and coworkers for supramolecular polymers formed by the homochiral metallosupramolecular polymer, which is prepared by complexing cholesteric-appended Schiff base ligands with $Zn^{2+}$ cations (compound **3**, as shown in Fig. 24a). The self-assembly of the resulting complexes can form different aggregates with different morphologies and CPL activity that changes with time. These kinetic changes, involving CPL-inversion and fluorescence colour switching, have been harnessed to encrypt information. To illustrate this effect, two different experiments were carried out. In the first experiment, a tulip flower with the $\mathbf{3}\cdot Zn^{2+}$ complex exhibited a time-dependent fluorescence transition from cyan to blue within 60 s (Fig. 24b). In the second experiment, a display able to generate a QR code was built with two inks, ink 1, which remains inert (no readable information), and ink 2, containing the $\mathbf{3}\cdot Zn^{2+}$ complex that gradually reveals the encoded data over time, representing an active or "enabled"

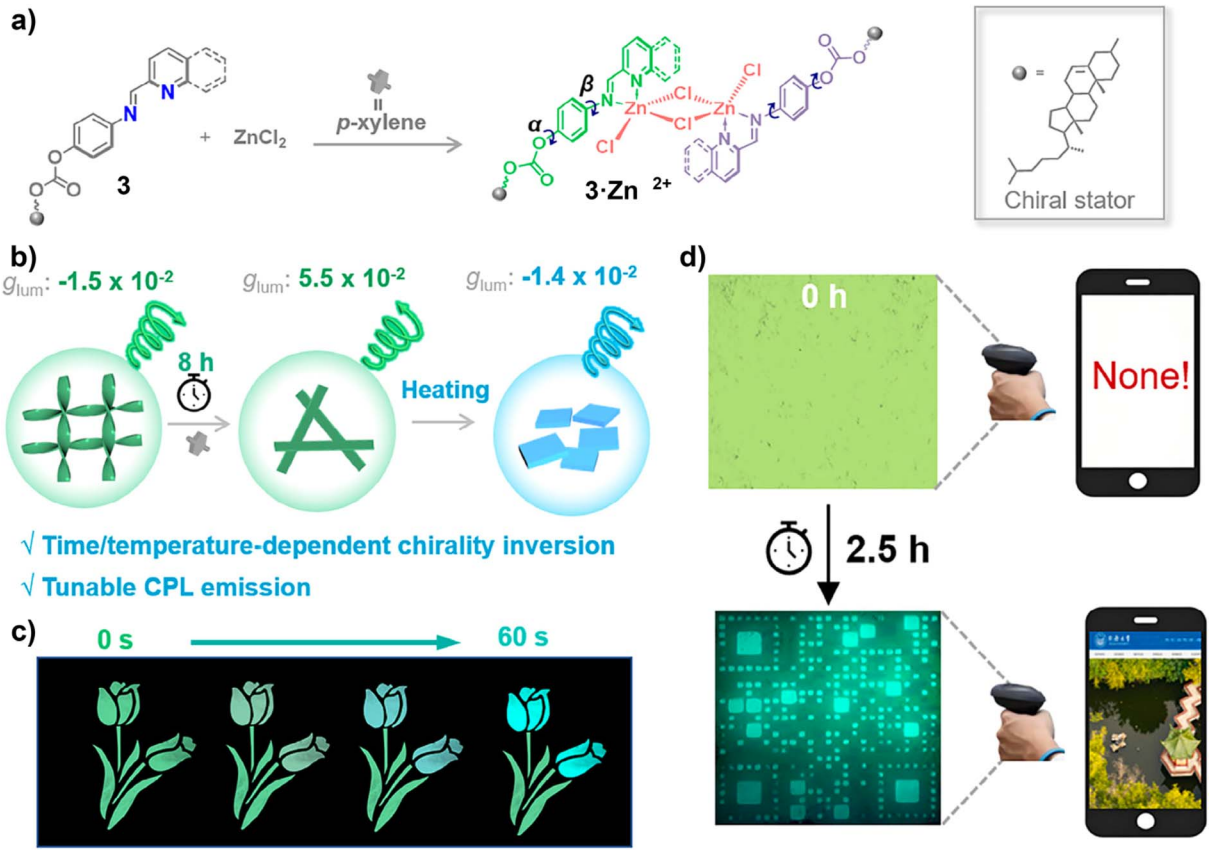


Fig. 24 (a) Chemical structure of the complexes formed by Schiff base **3** and $Zn^{2+}$; (b) schematic of the conformation transformation inducing dynamic multiple chirality inversion and tuneable CPL; and (c) and (d) design principle of time-dependent information encryption: (c) solid-state material demonstration of fluorescence changes in response to time and temperature of **3**·$Zn^{2+}$ complex aggregates at 385 K and (d) solid-state material demonstration of completely spontaneous time-dependent fluorescence changes of **3**·$Zn^{2+}$ complex aggregates and their application in a dynamic QR code display (reproduced from ref. 17a with permission from Wiley-VCH, Copyright 2025).

state. The changes in the supramolecular polymers formed by the **3**·$Zn^{2+}$ complex induce emission changes that reveal the complete QR code (Fig. 24c).[17a]

These applications of CPL-active supramolecular polymers exemplify the outstanding future of these chiral aggregated species.

## Conclusions

The research field of supramolecular polymers is highly active, with systems of ever-increasing complexity continually being developed. Mathematical models designed to study SP formation have played a key role in uncovering new approaches and functionalities for these self- or co-assembled supramolecular species. Within this broad field, chiral SPs represent a particularly valuable benchmark, as they enable the generation of helical structures that can model the origin of homochirality in nature and give rise to other compelling functionalities. Intriguingly, the presence of emissive moieties in the monomeric units constituting these chiral SPs can yield emissive aggregates that can also behave as CPL-active species. This property endows chiral SPs with additional interest in different research fields and applications. In this review, we highlight relevant examples of the different strategies utilized to achieve CPL-active supramolecular polymers. These strategies encompass decoration with monomeric units of elements of asymmetry (point or axial chirality) and the presence of metallic species. In all the examples of CPL-active supramolecular polymers collected in this review, the influence of external stimuli such as light, solvent, and temperature demonstrates the versatility of these supramolecular systems in affording CPL-active materials with remarkable dissymmetry factor ($g_{lum}$) and CPL brightness ($B_{CPL}$) values. Several examples of CPL-active metallo-organic SPs and purely organic systems are summarized, together with the outstanding applications of these CPL-active SPs as active layers in optoelectronic devices, anticounterfeiting, and encryption.

## Author contributions

Carmen Atienza and Fátima García: visualization, investigation and writing – original draft, review and Luis Sánchez: conceptualization, supervision, writing – original draft, review.

## Conflicts of interest

There are no conflicts to declare.

## Data availability

No primary research results, software or code have been included, and no new data were generated or analysed as part of this review.

## Acknowledgements

Financial support by the MCIN/AEI of Spain (PID2023-146971NB-I00) is acknowledged.

## Notes and references

1 Relevant reviews on supramolecular polymers: (*a*) L. Brunsveld, B. J. B. Folmer, E. W. Meijer and R. P. Sijbesma, *Chem. Rev.*, 2001, **101**, 4071; (*b*) M. Wehner and F. Würthner, *Nat. Rev.*, 2019, **4**, 38; (*c*) L. Yang, X. Tan, Z. Wang and X. Zhang, *Chem. Rev.*, 2015, **115**, 7196.

2 (*a*) T. Aida, A. Takemura, M. Fuse and S. Inoue, *J. Chem. Soc. Chem. Commun.*, 1988, **5**, 391; (*b*) C. Fouquey, J.-M. Lehn and A.-M. Levelut, *Adv. Mater.*, 1990, **2**, 254; (*c*) R. P. Sijbesma, F. H. Beijer, L. Brunsveld, B. J. B. Folmer, J. H. K. K. Hirschberg, R. F. M. Lange, J. K. L. Lowe and E. W. Meijer, *Science*, 1997, **278**, 1601.

3 (*a*) T. Aida, E. W. Meijer and S. I. Stupp, *Science*, 2012, **335**, 813; (*b*) Z. Alvarez, A. N. Kolberg-Edelbrock, I. R. Sasselli, J. A. Ortega, R. Qiu, Z. Syrgiannis, P. A. Mirau, F. Chen, S. M. Chin, S. Weigand, E. Kiskinis and S. I. Stupp, *Science*, 2021, **374**, 848; (*c*) O. Dumele, L. Đordevic, H. Sai, T. J. Cotey, M. H. Sangji, K. Sato, A. J. Dannenhoffer and S. I. Stupp, *J. Am. Chem. Soc.*, 2022, **144**, 3127; (*d*) W. Zhao, J. Tropp, B. Qiao, M. Pink, J. D. Azoulay and A. H. Flood, *J. Am. Chem. Soc.*, 2020, **142**, 2579; (*e*) Y. Yanagisawa, Y. Nan, K. Okuro and T. Aida, *Science*, 2018, **359**, 72; (*f*) Y. Yamamoto, T. Fukushima, Y. Suna, N. Ishii, A. Saeki, S. Seki, S. Tagawa, M. Taniguchi, T. Kawai and T. Aida, *Science*, 2006, **314**, 1761; (*g*) R. Chen, A. Hammoud, P. Aoun, M. A. Martínez-Aguirre, N. Vanthuyne, R. Maruchenko, P. Brocorens, L. Bouteiller and M. Raynal, *Nat. Commun.*, 2024, **15**, 4116.

4 (*a*) A. R. A. Palmans and E. W. Meijer, *Angew. Chem., Int. Ed.*, 2007, **46**, 8948; (*b*) F. García, R. Gómez and L. Sánchez, *Chem. Soc. Rev.*, 2023, **52**, 7524.

5 J. P. Riehl and F. S. Richardson, *Chem. Rev.*, 1986, **86**, 1.

6 (*a*) H. Tanaka, Y. Inoue and T. Mori, *ChemPhotoChem*, 2018, **2**, 386; (*b*) B. Doistau, J.-R. Jiménez and C. Piguet, *Front. Chem.*, 2020, **8**, 555; (*c*) L. Di B. Arrico and F. Zinna, *Chem. Eur. J.*, 2021, **27**, 2920.

7 K.-L. Wong, J.-C. G. Bünzli and P. A. Tanner, *J. Lumin.*, 2020, **224**, 117256.

8 C. A. Emeis and L. J. Oosterhoff, *Chem. Phys. Lett.*, 1967, **1**, 129.

9 Y. Chen, *Mater. Today Chem.*, 2022, **23**, 100651.

10 (*a*) J. Kumar, T. Nakashima and T. Kawai, *J. Phys. Chem. Lett.*, 2015, **6**, 3445; (*b*) H. Yan, Y. He, D. Wang, T. Han and B. Z. Tang, *Aggregate*, 2023, **4**, e331.

11 (*a*) Y. Sang, J. Han, T. Zhao, P. Duan and M. Liu, *Adv. Mater.*, 2020, **32**, 1900110; (*b*) R. D. Mukhopadhyay and A. Ajayaghosh, *Chem. Soc. Rev.*, 2023, **52**, 8635.

12 S. Datta, H. Itabashi and T. S. S. Yagai, *Nat. Chem.*, 2025, **17**, 477.

13 Y. D. Karmakar, P. Khanra, B. Ghosh, L. Roy and A. Das, *Small*, 2026, e12262.

14 (*a*) L. A. Estroff and A. D. Hamailton, *Chem. Rev.*, 2004, **104**, 1201; (*b*) N. M. Sangeetha and U. Maitra, *Chem. Soc. Rev.*, 2005, **34**, 821; (*c*) J. L. Lunkley, D. Shirotani, K. Yamanari, S. Kaizaki and G. Muller, *J. Am. Chem. Soc.*, 2008, **130**, 13814; (*d*) F. Zinna, U. Giovanella and L. Di Bari, *Adv. Mater.*, 2015, **27**, 1791; (*e*) T. Ikeda, M. Takayama, J. Kumar, T. Kawai and T. Haino, *Dalton Trans.*, 2015, **44**, 1356; (*f*) Y. B. Tan, Y. Okayasu, S. Katao, Y. Nishikawa, F. Asanoma, M. Yamada, J. Yuasa and T. Kawai, *J. Am. Chem. Soc.*, 2020, **142**, 17653; (*g*) X.-Y. Luo and M. Pan, *Coord. Chem. Rev.*, 2022, **468**, 21640; (*h*) M. Tsurui, R. Takizawa, Y. Kitagawa, M. Wang, M. Kobayashi, T. Taketsugu and Y. Hasegawa, *Angew. Chem., Int. Ed.*, 2024, **63**, e202405584.

15 D. Niu, Y. Jiang, L. Ji, G. Ouyang and M. Liu, *Angew. Chem., Int. Ed.*, 2019, **58**, 5946.

16 (*a*) G. Liu, J. Sheng, W. L. Teo, G. Yang, H. Wu, Y. Li and Y. Zhao, *J. Am. Chem. Soc.*, 2018, **140**, 16275; (*b*) K. Fu and G. Liu, *Chem. Commun.*, 2023, **59**, 13751; (*c*) L. Yao, K. Fu, X. Wang, M. He, W. Zhang, P.-Y. Liu, Y. P. He and G. Liu, *ACS Nano*, 2023, **17**, 2159; (*d*) K. Fu, D.-H. Qu and G. Liu, *J. Am. Chem. Soc.*, 2024, **146**, 33832.

17 (*a*) M. He, P. Chen, Q. Wang, S. Zheng, C. Zhang, D.-H. Qu and G. Liu, *Adv. Funct. Mater.*, 2025, e10772; (*b*) M. He, H. Su, L. Zhu and G. Liu, *Chem. Mater.*, 2024, **36**, 2508.

18 G. Zou, Z. Jiang, D. Li, Q. Li and Y. Cheng, *Chem. Sci.*, 2024, **15**, 18534.

19 X. Niu, X. Ou, S. Ren, K. Wang, F. Song, X. Dong, W.-J. Guo, H.-Q. Peng, Z. Zhao, J. W. Y. Lam, Y. S. Zhao, F. Li, S.-Y. Yu and B. Z. Tang, *Aggregate*, 2025, **6**, e70003.

20 A. Gopal, M. Hifsudheen, S. Furimi, M. Takeuchi and A. Ajayaghosh, *Angew. Chem., Int. Ed.*, 2012, **51**, 1.

21 J. Kumar, T. Nakashima, H. Tsumatori, M. Mori, M. Naito and T. Kawai, *Chem. Eur. J.*, 2013, **19**, 14090.

22 L. López-Gandul, C. Naranjo, C. Sánchez, R. Rodríguez, R. Gómez, J. Crassous and L. Sánchez, *Chem. Sci.*, 2022, **13**, 11577.

23 Y. Xue, C. Zhang, T. Lv, L. Qiu and F. Wang, *Angew. Chem., Int. Ed.*, 2023, **62**, e202300972.

24 (*a*) X. Shang, I. Song, H. Ohtsu, Y. H. Lee, T. Zhao, T. Kojima, J. H. Jun, M. Kawano and J. H. Oh, *Adv. Mater.*, 2017, **29**, 1605828; (*b*) M. Schulz, F. Balzer, D. Scheunemann, O. Arteaga, A. Lützen, S. C. J. Meskers and M. Schiek, *Adv. Funct. Mater.*, 2019, **29**, 1900684; (*c*) X. Shang, I. Song, J. H. Lee, W. Choi, J. Ahn, H. Ohtsu, J. C. Kim, J. Y. Koo, S. K. Kwak and J. H. Oh, *ACS Nano*, 2020, **14**, 14146–14156; (*d*) L. Liu, Y. Yang, Y. Wang, M. A. Adil, Y. Zhao, J. Zhang, K. Chen, D. Deng, H. Zhang, K. Amin, Y. Wu, Y. Zhang and Z. Wei, *ACS Mater. Lett.*, 2022, **4**, 401.

 

25 W. Yuan, L. Chen, Ch. Yuan, Z. Zhang, X. Chen, X. Zhang, J. Guo, Ch. Qian, Z. Zhao and Y. Zhao, *Nat. Commun.*, 2023, **14**, 8022.
26 L. Gao, R. Liao, L. Ao, Y. Zhang, J. Jin and F. Wang, *Angew. Chem., Int. Ed.*, 2025, **64**, e202505776.
27 Y. Guo, Y. Zhan, J. Ma, R. Liao and F. Wang, *Nat. Commun.*, 2024, **15**, 9303.
28 T.-A. Cucuiet, A. Vargas Jentzsch, F. Picini, M. Maaloum, G. Raffy, E. Moulin, D. M. Bassani and N. Giuseppone, *Angew. Chem., Int. Ed.*, 2025, e202516824.
29 S. Patra, S. Dhiman and S. J. George, *Chem. Mater.*, 2024, **36**, 9460.
30 (*a*) J. Crassous, I. G. Stará and I. Starý, *Helicenes – Synthesis, Properties and Applications*, Wiley, 2022; (*b*) C.-F. Chen and Y. Shen, in *Helicene Chemistry: From Synthesis to Applications*, Springer: Berlin, Heidelberg, 2017; (*c*) M. Gingras, *Chem. Soc. Rev.*, 2013, **42**, 968; (*d*) Y. Shen and C.-F. Chen, *Chem. Rev.*, 2012, **112**, 1463; (*e*) K. Dhbaibi, L. Favereau and J. Crassous, *Chem. Rev.*, 2019, **119**, 8846.
31 (*a*) K. Dhbaibi, L. Abella, S. Meunier-Della-Gatta, T. Roisnel, N. Vanthuyne, B. Jamoussi, G. Pieters, B. Racine, E. Quesnel, J. Autschbach, J. Crassous and L. Favereau, *Chem. Sci.*, 2021, **12**, 5522; (*b*) M. J. Narcis and N. Takenaka, *Eur. J. Org Chem.*, 2014, 21; (*c*) D. Schweinfurth, M. Zalibera, M. Kathan, C. Shen, M. Mazzolini, N. Trapp, J. Crassous, G. Gescheidt and F. Diederich, *J. Am. Chem. Soc.*, 2014, **136**, 13045; (*d*) E. Anger, M. Srebro, N. Vanthuyne, L. Toupet, S. Rigaut, C. Roussel, J. Autschbach, J. Crassous and R. Réau, *J. Am. Chem. Soc.*, 2012, **134**, 15628; (*e*) T. Verbiest, S. V. Elshocht, M. Kauranen, L. Hellemans, J. Snauwaert, C. Nuckolls, T. J. Katz and A. Persoons, *Science*, 1998, **282**, 913.
32 T. Kaseyama, S. Furumi, X. Zhang, K. Tanaka and M. Takeuchi, *Angew. Chem., Int. Ed.*, 2011, **50**, 3684.
33 M. Li, C. Zhang, L. Fang, L. Shi, Z. Tang, H.-Y. Lu and C.-F. Chen, *ACS Appl. Mater. Interfaces*, 2018, **10**, 8225.
34 C. Shen, F. Gan, G. Zhang, Y. Ding, J. Wang, R. Wang, J. Crassous and H. Qiu, *Mater. Chem. Front.*, 2020, **4**, 837.
35 (*a*) R. Rodríguez, C. Naranjo, A. Kumar, P. Matozzo, T. Kumar Das, Q. Zhu, N. Vanthuyne, R. Gómez, R. Naaman, L. Sánchez and J. Crassous, *J. Am. Chem. Soc.*, 2022, **144**, 7709; (*b*) R. Rodríguez, C. Naranjo, A. Kumar, K. Dhbaibi, P. Matozzo, F. Camerel, N. Vanthuyne, R. Gómez, R. Naaman, L. Sánchez and J. Crassous, *Chem. – Eur. J.*, 2023, **29**, e202302254.
36 P. A. Korevaar, C. Schaefer, T. F. A. de Greef and E. W. Meijer, *J. Am. Chem. Soc.*, 2012, **134**, 13482.
37 L. López-Gandul, R. Rodríguez, N. Vanthuyne, J. Crassous and L. Sánchez, *Nanoscale*, 2024, **16**, 13041.
38 G. Bringmann, T. Gulder, T. A. M. Gulder and M. Breuning, *Chem. Rev.*, 2011, **111**, 563.
39 (*a*) H. Maeda, Y. Bando, K. Shimomura, I. Yamada, M. Naito, K. Nobusawa, H. Tsumatori and T. Kawai, *J. Am. Chem. Soc.*, 2011, **133**, 9266; (*b*) E. M. Sánchez-Carnerero, F. Moreno, B. L. Maroto, A. R. Agarrabeitia, M. J. Ortiz, B. G. Vo, G. Muller and S. de La Moya, *J. Am. Chem. Soc.*, 2014, **136**, 3346.
40 F. Würthner, C. R. Saha-Möller, B. Fimmel, S. Ogi, P. Leowanawat and D. Schmidt, *Chem. Rev.*, 2016, **116**, 962.
41 J. Kumar, T. Nakashima, H. Tsumatori and T. Kawai, *J. Phys. Chem. Lett.*, 2014, **5**, 316.
42 J. Kumar, H. Tsumatori, J. Yuasa, T. Kawai and T. Nakashima, *Angew. Chem., Int. Ed.*, 2015, **54**, 5943.
43 Y. Sheng, D. Shen, W. Zhang, H. Zhang, C. Zhu and Y. Cheng, *Chem. Eur. J.*, 2015, **21**, 13196.
44 D. Deb, M. Parashar, S. Sarkar, S. Ghosh, S. Balasubramanian and S. J. George, *Angew. Chem., Int. Ed.*, 2025, e20385.
45 F. Lin, X. Zhang, J. Zhao, S. Shi, D. Liu, K. Wang, Z. Geng, F. Song, F. Li and B. Z. Tang, *Angew. Chem., Int. Ed.*, 2025, e15768.
46 C. Du, Z. Li, X. Zhu, G. Ouyang and M. Liu, *Nat. Comm.*, 2022, **17**, 1294.
47 J. Han, D. Yang, X. Jin, Y. Jiang, M. Liu and P. Duan, *Angew. Chem., Int. Ed.*, 2019, **58**, 7013.
48 H. Zhang, J. Han, X. Jin and P. Duan, *Angew. Chem., Int. Ed.*, 2021, **60**, 4575.
49 (*a*) S. Tadepalli, J. M. Slocik, M. K. Gupta, R. R. Naik and S. Singamaneni, *Chem. Rev.*, 2017, **117**, 12705; (*b*) D.-W. Zhang, M. Li and C.-F. Chen, *Chem. Soc. Rev.*, 2020, **49**, 1331.
50 (*a*) E. Peeters, M. P. T. Christiaans, R. A. J. Janssen, H. F. M. Schoo, H. P. J. M. Dekkers and E. W. Meijer, *J. Am. Chem. Soc.*, 1997, **119**, 9909; (*b*) Y. Geng, A. Trajkovska, S. W. Culligan, J. J. Ou, H. M. P. Chen, D. Katsis and S. H. Chen, *J. Am. Chem. Soc.*, 2003, **125**, 14032.
51 (*a*) G. Lu, Z.-G. Wu, R. Wu, X. Cao, L. Zhou, Y.-X. Zheng and C. Yang, *Adv. Funct. Mater.*, 2021, **31**, 2102898; (*b*) J. R. Brandt, X. Wang, Y. Yang, A. J. Campbell and M. J. Fuchter, *J. Am. Chem. Soc.*, 2016, **138**, 9743.
52 Z. Geng, Z. Liu, H. Li, Y. Zhang, W. Zheng, Y. Quan and Y. Cheng, *Adv. Mater.*, 2023, **35**, 2209495.
53 R. Chowdhury, M. D. Preuss, H.-H. Cho, J. J. P. Thompson, S. Sen, T. K. Baikie, P. Ghosh, Y. Boeije, X. Wei Chua, K.-W. Chang, E. Guo, J. van der Tol, B. W. L. van den Bersselaar, A. Taddeucci, N. Daub, D. M. Dekker, S. T. Keene, G. Vantomme, B. Ehrler, S. C. J. Meskers, A. Rao, B. Monserrat, E. W. Meijer and R. H. Friend, *Science*, 2025, **387**, 1175.
54 Y.-X. Yuan, J.-H. Jia, Y.-P. Song, F.-Y. Ye, Y.-S. Zheng and S.-Q. Zang, *J. Am. Chem. Soc.*, 2022, **144**, 5389.
55 Y. Shi, J. Han, X. Jin, W. Miao, Y. Zhang and P. Duan, *Adv. Sci.*, 2022, **9**, 2201565.
56 S. Lin, S. Zeng, Z. Li, Q. Fan and J. Guo, *ACS Appl. Mater. Interfaces*, 2022, **14**, 30362.